

# Simultaneously search for multi-target Galactic binary gravitational waves in reduced parameter space with LMPSO-CV

Pin Gao,<sup>1</sup> Xi-Long Fan,<sup>2,\*</sup> and Zhou-Jian Cao<sup>1</sup>

<sup>1</sup>*Department of Astronomy, Beijing Normal University, Beijing 100875, China*

<sup>2</sup>*School of Physics and Technology, Wuhan University, Wuhan 430072, China*

We propose an innovative approach to the concurrent exploration of gravitational waves originating from Galactic binaries through the development of a new Local Maxima Particle Swarm Optimization (LMPSO) algorithm. Our methodology employs strategic Create Voids (CV) to streamline parameter space, maximizing the identification of local maxima for the  $\mathcal{F}$ -statistic even in the overlapped signals case. Subsequently, a “find-real- $\mathcal{F}$ -statistic-analysis”, which implements the astrophysical models and properties of  $\mathcal{F}$ -statistic in parameter space, is conducted to reveal Galactic binary gravitational wave signals within the dataset. Our new approach eliminates inaccuracies associated with signal subtraction contamination, which is a challenge for traditional iterative-subtraction method when addressing low signal-to-noise ratio signals (e.g.,  $\text{SNR} < 15$ ). We also consider the effect of overlapping signals and degeneracy noise. To demonstrate the efficacy of our approach, we utilize the residuals from the LISA mock data challenge (LDC1-4), where 10982 injection sources with  $\text{SNR} \geq 15$  have been eliminated. For the remaining low SNR sources ( $\text{SNR} < 15$ ), the LMPSO-CV method efficiently identifies 8995 signals with a 52.3% detection rate or 3463 signals with a 73.1% detection rate when the correlation coefficient threshold  $R_t$  is set to 0.8.

## I. INTRODUCTION

In the evolving landscape of ground-based gravitational wave (GW) detectors, recent observations [1–3] underscore advancements in sensitivity and increased detection distances, resulting in a surge of GW events [4, 5]. However, the inherent frequency limitations (10 Hz to 1000 Hz) of these detectors introduce a bias toward specific sources, such as stellar-mass binary black hole mergers, binary neutron star mergers, and neutron star-black hole mergers [6–8]. Despite their significance, these detections merely scratch the surface of the comprehensive GW spectrum. The quest for detecting GWs at alternative frequencies has prompted the exploration of kilohertz GWs [9, 10], lunar GW detection [11], space-based GW detection [12, 13], and the utilization of pulsar timing arrays [14–16]. Pulsar timing arrays, in particular, have yielded compelling evidence of potential signals in the extremely low-frequency range [17–19]. Beyond pulsar timing arrays, several space-based GW detection initiatives, including LISA [12, 13, 20], Taiji [21–24], and Tianqin [25–28], among others, are in preparation, expanding the horizons of gravitational wave research.

The Taiji program [21–24] and the LISA program [12, 13, 20] are positioned to establish space-based GW detectors strategically, with one located 20 degrees ahead and the other 20 degrees behind Earth’s orbit. Configured with arm lengths of approximately 3 million kilometers and 2.5 million kilometers, respectively, each detector consists of three independent satellites interconnected by laser links. Operating on the same fundamental principles as ground-based GW detectors, these instruments will measure minute spatial displacements

between pairs of satellites for GW detection. By evading ground-based seismic noise and possessing substantial arm lengths, space-based GW detectors exhibit sensitivities several orders of magnitude lower than their ground-based counterparts, covering a frequency range from about  $10^{-4}$  Hz to  $10^{-1}$  Hz. Within this frequency band, an array of GW sources is anticipated, including supermassive black hole mergers, Galactic binaries, and extreme mass ratio inspirals, among others [29]. Galactic binaries, especially double white dwarf (DWD) binaries, are expected to be abundant. According to current Galactic models, tens of millions to billions of Galactic binaries could emit nearly monochromatic GW signals within the sensitivity frequencies of LISA and Taiji [30]. The prevalence of these signals poses a significant challenge in signal resolution due to potential overlap. Additionally, as Galactic binary gravitational wave signals persist stably throughout the detection period, they have the potential to impact the analysis of other types of signals.

In recent decades, many data processing methods have emerged for analyzing GW signals from Galactic binaries [31–44]. Among these algorithms, LDC1-4 data (Radler) were utilized for testing in three different algorithms. The first algorithm employed RJMCMC’s global fit approach [37, 43], while the second utilized MCMC and GPU-accelerated techniques [39, 44], and the third implemented a PSO-based iterative-subtraction algorithm combined with a cross-validation approach [38, 42]. When applied to the LDC1-4 data, the first algorithm identified 826, 1819, 4356, and 7255 sources over periods of 1.5, 3, 6, and 12 months, respectively, with correlation coefficient  $R > 0.8$  [43]. The second algorithm detected 3407, 6251, and 10363 sources over periods of 6, 12, and 24 months, respectively, with  $R > 0.9$  [44]. The third algorithm identified 10341 sources over 24 months with  $R > 0.9$  [38]. Additionally, the per-

---

\* xilong.fan@whu.edu.cn

formance of the third algorithm was also evaluated on 3 and 6 months data, revealing the detection of 3010 and 5418 sources with  $R > 0.9$  (this evaluation was conducted without cross-validation, which could improve the detection rate but lead to the loss of some sources) [42]. Despite the efforts of these algorithms to target sources with  $\text{SNR} > 7$  or  $\text{SNR} > 10$ , there are still many sources that remain unsearched, given that there are approximately 27,000 injection sources with  $\text{SNR} > 7$  and 18,000 with  $\text{SNR} > 10$  for two-year detection. This scenario may arise due to several factors. Firstly, the presence of high SNR sources may overshadow the weaker low SNR signals during multi-source fitting, resulting in their neglect. Secondly, as the number of searched signals increases, the potential for inaccurate subtraction contamination from the iterative-subtraction algorithm in the data residual grows, impacting the detection of low SNR signals. Thirdly, the more serious overlap of low SNR signals poses a more significant challenge compared to high SNR signals, particularly in the absence of sufficient priors regarding the number of sources and the approximate parameter ranges. To alleviate these challenges, especially the second, we propose a non iterative-subtraction strategy and evaluate its performance in single-source fitting scenarios. We believe that our method holds advantages in low SNR and low-frequency regions characterized by higher source densities compared to high SNR and high-frequency regions.

Our objective is to accurately identify signals with  $\text{SNR} < 15$  (with respect to instrument noise) during the two-year detection period. While the iterative-subtraction strategy proves effective in scenarios where signals have  $\text{SNR} \geq 15$  [38, 42], benefiting from relatively sparse signal density and high SNR, its efficacy gradually diminishes as the SNR decreases. We propose a novel search strategy capable of simultaneously detecting multiple Galactic binaries, and implement it using LDC1-4 data. Before initiating the search, assuming a method exists to eliminate signals with  $\text{SNR} \geq 15$ , we begin by subtracting all injection sources with  $\text{SNR} \geq 15$  from the LDC1-4 data. Subsequently, we proceed with our method within the residual data. Our algorithm is designed to identify as many local maxima of the  $\mathcal{F}$ -statistic surpassing a specified threshold as possible in parameter space. Following this, we analyze the results and extract signal parameters from these local maxima.

The structure of this article is organized as follows: In Sec. II, we provide an introduction to the gravitational waveform of DWD binaries and the response function of the LISA detector, both based on the LDC1-4 data. Sec. III explores the distribution of the  $\mathcal{F}$ -statistic when single or multiple signals coexist in LISA data, leading to the generation of degeneracy noise. Sec. IV outlines the LMPSO-CV method utilized for searching the local maxima of the  $\mathcal{F}$ -statistic, incorporating a specially developed Local Maxima Particle Swarm Optimization (LMPSO) algorithm and a technique for reducing parameter space to prevent redundant searches for the same po-

sition in parameter space—referred to as “create voids” (CV). In Sec. V, we elaborate on how to analyze these local maxima with the “find-real- $\mathcal{F}$ -statistic-analysis”, focusing on removing a significant amount of degeneracy noise and mitigating instrument noise. Sec. VI presents the results in terms of the detection rate and SNR, along with the parameter errors and computational time. Conclusions are drawn in Sec. VII. In Appendix A, we present the results of the case search. In Appendix B, we discuss the presence of overlapping signals within LDC1-4 injection sources, which complicates the search process.

## II. DATA DESCRIPTION

We utilize the LISA mock data challenge released in 2019 (LDC1-4) [45]. This dataset encompasses around 30 million binary systems, accompanied by simulated LISA instrument noise, and employs a signal sampling period of 15 seconds. The complete dataset spans a total duration of two years, equivalent to 62,914,560 seconds.

### A. Galactic binaries distribution

Galactic binary gravitational waves in the source frame are defined as:

$$\begin{aligned} h_+(t) &= \mathcal{A} (1 + \cos^2 \iota) \cos \Phi(t), \\ h_\times(t) &= -2\mathcal{A} \cos \iota \sin \Phi(t), \\ \Phi(t) &= \phi_0 + 2\pi f t + \pi \dot{f} t^2, \end{aligned} \quad (1)$$

where  $\mathcal{A}$  represents the GW amplitude,  $\iota$  represents the Galactic binary orbit to the line of sight from the Solar System barycentric (SSB) origin,  $\phi_0$  represents the initial phase.  $f$  is the GW frequency, and  $\dot{f}$  is the first order derivative of  $f$ . Incorporating the polarization, denoted as  $\psi$ , from  $h_+$  and  $h_\times$ , along with two positional parameters—Ecliptic Latitude  $\beta$  and Ecliptic Longitude  $\lambda$ —constitutes a total of eight parameters that characterize a Galactic binary system.

There are 29857650 Galactic binaries in LDC1-4 data, but only 27680 with  $\text{SNR} > 7$  in two-year detection. Among these, there are 10982 binaries with  $\text{SNR} > 15$ , which are sources that most of them can already solved good by current search methods. For the remaining 16698 sources, detection is more difficult because they are mainly concentrated in low ( $f < 1 \times 10^{-3}$  Hz) and medium ( $1 \times 10^{-3}$  Hz  $< f < 4 \times 10^{-3}$  Hz) frequencies with a high density and are more susceptible to instrument noise.

Fig. 1 illustrates the distribution of binaries in the galactic coordinate system, with the majority congregating on the Galactic Disk. Less than one percent of binaries exhibit a Galactic Latitude outside the range of -0.5 rad to 0.5 rad. In Fig. 2, we depict the frequency distribution of binaries. Most binaries with  $\text{SNR} > 15$  are readily

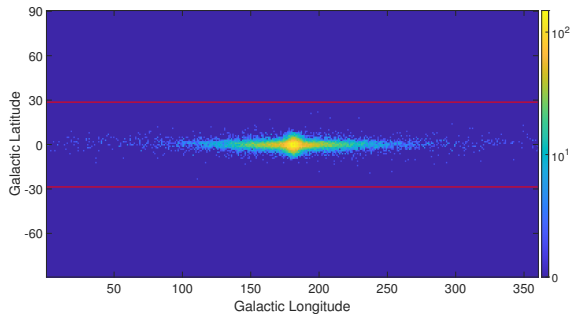


Figure 1. Galactic binaries distribution in the galactic coordinate system of LDC1-4 ( $\text{SNR} > 7$ ). The color bar represents the number of binaries within one square degree on the celestial sphere. The two red lines mark the area where the Galactic Latitude is between  $-0.5$  rad and  $0.5$  rad ( $-28.65^\circ \sim 28.65^\circ$ ), and there are 27,436 binaries in this area out of 27,680 binaries in total. This prior information will be used in the data analysis (See Sec. VB3 for details).

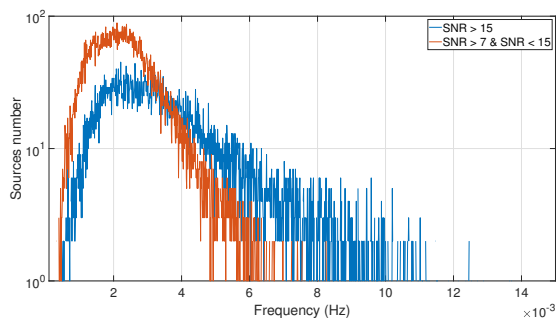


Figure 2. Distribution of Galactic binaries in different frequency bins of the LDC1-4 data. Each bin has a width of 0.01 mHz. We categorize the signals into two groups based on SNR: those with  $\text{SNR} > 15$  and those with  $7 < \text{SNR} < 15$ . In the figure, we observe that binaries are more concentrated at low frequencies ( $f < 1 \times 10^{-3}$  Hz) and medium frequencies ( $1 \times 10^{-3}$  Hz  $< f < 4 \times 10^{-3}$  Hz) when considering signals with  $7 < \text{SNR} < 15$ .

resolvable using current search methods. In contrast, binaries with  $7 < \text{SNR} < 15$  exhibit higher densities at low frequencies ( $f < 1 \times 10^{-3}$  Hz) and medium frequencies ( $1 \times 10^{-3}$  Hz  $< f < 4 \times 10^{-3}$  Hz), posing challenges for effective discrimination. Given our primary focus on signals with low SNR ( $\text{SNR} < 15$ ), we initiate the process by subtracting binary waveforms with  $\text{SNR} > 15$  from the raw data.

### B. Space-based GW detector response

Due to the significant influence of laser phase noise on GW signals, space-based GW detectors employ a technique known as time-delay interferometry (TDI). This method involves the combination of data from different arms to alleviate the impact of laser phase noise.

In the LDC1-4 data, the first-generation TDI Michelson combinations, denoted as  $X$ ,  $Y$ ,  $Z$ , are utilized. This first-generation TDI assumes constant distances between spacecraft, treating them as a rigid body [46–49]. We recombine the three channels  $X$ ,  $Y$ ,  $Z$  into  $A$ ,  $E$ ,  $T$  channels to ensure that instrument noises are uncorrelated:

$$\begin{aligned} A &= \frac{Z - X}{\sqrt{2}}, \\ E &= \frac{X - 2Y + Z}{\sqrt{6}}, \\ T &= \frac{X + Y + Z}{\sqrt{3}}. \end{aligned} \quad (2)$$

The development of a comprehensive response for a space-based gravitational wave detector is a complex task, requiring consideration of intricate details related to the detectors' orbits. In this regard, we rely on the formulation presented in Ref. [36], a model that has demonstrated high effectiveness in previous studies [36, 38, 42].

While the gravitational wave (GW) emitted by a Galactic binary inherently exhibits a monochromatic waveform, the Doppler effect introduces frequency broadening due to the orbital motion of the detector. The Earth, moving at a velocity of approximately 30 km/s around the SSB, shares a similar speed with LISA. As expressed by the Doppler effect formula,  $f_1 = f \times \frac{c \pm v}{c}$  (where  $c$  is the speed of light), the GW frequency undergoes a shift of approximately 0.01% in one frequency direction (this is a maximum, and the specific shift depends on the location of the GW source).

## III. PARAMETER DEGENERACY

### A. $\mathcal{F}$ -statistic

The Galactic binary GW of the first-generation TDI Michelson observable  $X$  is given by a linear combination of the four time-dependent functions  $h^{(k)}(t)$ .

$$h(t) = 2\omega L \sin(\omega L) \sum_{k=1}^4 a^{(k)} h^{(k)}(t), \quad (3)$$

where  $\omega$  is the angular GW frequency and  $L$  is the arm length of LISA.  $a^{(k)} = (a^{(1)}, a^{(2)}, a^{(3)}, a^{(4)})$  is the reparametrization of four extrinsic parameters  $\mathcal{A}$ ,  $\phi_0$ ,  $\psi$  and  $\iota$ .  $h^{(k)}(t)$  is a matrix of template waveforms and it depends on the four remaining intrinsic parameters:  $f$ ,  $\dot{f}$ ,  $\beta$  and  $\lambda$ .

The  $\mathcal{F}$ -statistic is proposed to search for monochromatic GWs [50]. Supposing there is a Galactic binary GW in the data, the detector's data in  $X$  can be expressed as

$$s(t) = n(t) + h(t), \quad (4)$$

where  $n(t)$  is the instrument noise and  $h(t)$  is LISA response GW. The log likelihood function has the form

$$\ln \Lambda = (s | h) - \frac{1}{2}(h | h), \quad (5)$$

where the scalar product  $( | )$  is defined by

$$(x | y) := 4 \operatorname{Re} \int_0^\infty \frac{\tilde{x}(f)\tilde{y}^*(f)}{S_h(f)} df. \quad (6)$$

The symbol  $\tilde{\phantom{x}}$  represents the Fourier transform,  $*$  denotes complex conjugation, and  $S_h$  represents the one-sided spectral density of the detector's noise.

It maximizes the log-likelihood function  $\ln \Lambda$  concerning parameters  $a^{(k)}$ , by solving

$$\frac{\partial \ln \Lambda}{\partial a^{(k)}} = 0. \quad (7)$$

Then it substitutes the maximum likelihood estimators  $\hat{a}^{(k)}$  in  $\ln \Lambda$  yielding the reduced log-likelihood function denoted by  $\mathcal{F}$ -statistic. One finds the  $\mathcal{F}$ -statistic maxima in the intrinsic parameter space and then obtains four extrinsic parameters through analytic expression (see [36] for more details). The expectation of the  $\mathcal{F}$ -statistic is

$$E[2\mathcal{F}] = 4 + \rho^2, \quad (8)$$

where  $\rho$  is SNR, and

$$\rho^2 = \sum_I \left( \|\tilde{S}^I(\theta)\|^I \right)^2, I \in \{A, E, T\}. \quad (9)$$

### B. The frequency-position parameter degeneracy

Due to the inherent nature of the  $\mathcal{F}$ -statistic as a matching filtering method, employing a LISA response GW waveform to correlate with the signal in LISA data yields a  $\mathcal{F}$ -statistic value that exceeds instrument noise levels if the two waveforms share the same Doppler modulating frequency at the same time. This results in the frequency-position parameter degeneracy. In Fig. 3, the  $x - y$  coordinate plane denotes the ecliptic plane, with the  $x$ -axis directed toward the vernal equinox. LISA orbits the SSB with a velocity vector  $\vec{v}$  within the ecliptic plane (this is a simplified model and does not include cartwheel motions of LISA), and the SSB is positioned at the origin ( $o$ ). Assuming binary  $A$  is the signal in the LISA data,  $f_A$  represents binary  $A$ 's frequency relative to the SSB. Due to the orbital motion of LISA, the frequency  $f_A$ , modulated by the Doppler effect  $f_{A_{\text{do}}}$  in the LISA data, can be expressed as

$$f_{A_{\text{do}}} = f_A \frac{c + \nu_A}{c}, \quad (10)$$

where

$$\nu_A = |\vec{v}| \sin(\lambda_A - \lambda_0) \cos \beta_A \quad (11)$$

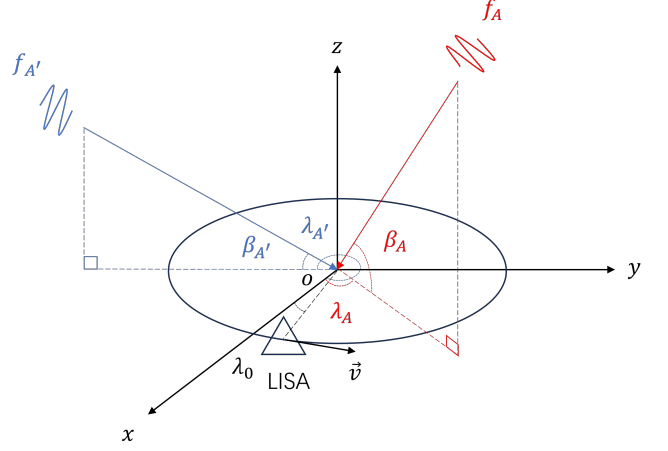


Figure 3. The  $x - y$  coordinate plane represents the ecliptic plane, with the  $x$ -axis directed toward the vernal equinox. LISA orbits the SSB within the ecliptic plane at a speed denoted by  $\vec{v}$ , and the origin  $o$  corresponds to the SSB's position. Within the LISA data, there exists a GW signal originating from binary  $A$  with parameters  $f_A$ ,  $\beta_A$  and  $\lambda_A$ . Employing a match filtering method, such as the  $\mathcal{F}$ -statistic, for detection involves assuming that the matched waveform corresponds to binary  $A'$  ( $f_{A'}$ ,  $\beta_{A'}$ ,  $\lambda_{A'}$ ).

represents the velocity of LISA relative to binary  $A$ , while  $\lambda_0$  denotes LISA's Ecliptic Longitude at the given time. Additionally,  $\lambda_A$  represents the Ecliptic Longitude of binary  $A$ , and  $\beta_A$  represents its Ecliptic Latitude.

Assuming we use binary  $A'$  as the match waveform, due to the Doppler effect of LISA orbit motion,  $f_{A'_{\text{do}}}$  is its LISA response frequency

$$f_{A'_{\text{do}}} = f_{A'} \frac{c + \nu_{A'}}{c}, \quad (12)$$

where

$$\nu_{A'} = |\vec{v}| \sin(\lambda_{A'} - \lambda_0) \cos \beta_{A'}. \quad (13)$$

$\lambda_{A'}$  and  $\beta_{A'}$  are the Ecliptic Longitude and Ecliptic Latitude of binary  $A'$ , respectively. Making these two modulated frequencies equal ( $f_{A_{\text{do}}} = f_{A'_{\text{do}}}$ ), we can get the equation

$$f_A [c + |\vec{v}| \sin(\lambda_A - \lambda_0) \cos \beta_A] = f_{A'} [c + |\vec{v}| \sin(\lambda_{A'} - \lambda_0) \cos \beta_{A'}]. \quad (14)$$

Let  $\theta = \lambda_A - \lambda_0$ . Therefore,  $\lambda_{A'} - \lambda_0 = \theta + (\lambda_{A'} - \lambda_A)$ . The above equation can be

$$f_{A'} = f_A \frac{c + |\vec{v}| \sin \theta \cos \beta_A}{c + |\vec{v}| \sin(\theta + \lambda_{A'} - \lambda_A) \cos \beta_{A'}}. \quad (15)$$

This equation pertains to the presence of a GW signal from binary  $A$  in LISA data. When employing the  $\mathcal{F}$ -statistic to detect the signal, it describes the distribution of the  $\mathcal{F}$ -statistic in the parameter space.



Considering the aforementioned equation, if the LISA data contains a signal with the frequency  $f_A$  relative to the SSB, the maximum frequency  $f_{A'_{\max}}$  in the  $\mathcal{F}$ -statistic degeneracy is

$$f_{A'_{\max}} = f_A \frac{c + |\vec{v}|}{c - |\vec{v}|} \approx 1.0002 \times f_A \quad (16)$$

when  $\theta = \frac{\pi}{2}$ ,  $\lambda_{A'} - \lambda_A = \pi$ , and  $\beta_A = \beta_{A'} = 0$ . Similarly, the minimum frequency  $f_{A'_{\min}}$  in the  $\mathcal{F}$ -statistic degeneracy is

$$f_{A'_{\min}} = f_A \frac{c - |\vec{v}|}{c + |\vec{v}|} \approx 0.9998 \times f_A \quad (17)$$

when  $\theta = -\frac{\pi}{2}$ ,  $\lambda_{A'} - \lambda_A = \pi$ , and  $\beta_A = \beta_{A'} = 0$ . It determines the frequency range  $[f_{A'_{\min}}, f_{A'_{\max}}]$  of the  $\mathcal{F}$ -statistic degeneracy generated by the GW signal which has frequency  $f_A$  relative to the SSB. Eq. 16 and 17 show the frequency range of the  $\mathcal{F}$ -statistic degeneracy generated by the  $f_A$  signal is proportional to  $f_A$  itself. This results in higher  $f_A$  exhibiting a more extensive distribution of the  $\mathcal{F}$ -statistic, while lower  $f_A$  presents a narrower frequency distribution for the  $\mathcal{F}$ -statistic.

We selected a set of parameters from the LDC1-4 injection sources catalog and assigned them to binary  $A$ , with the specific parameter values detailed in Tab. III (Appendix A). The  $\mathcal{F}$ -statistic degeneracy originating from binary  $A$  is plotted in Fig. 4. In Fig. 4(a),  $\beta_{A'} = \beta_A$ , and in Fig. 4(b),  $\lambda_{A'} = \lambda_A$ . We utilized a spatial resolution of  $\pi/40$  radians in the figures.  $\theta$  represents the angle between LISA and binary  $A$ , providing a representation of LISA at various positions in its orbit. The  $\mathcal{F}$ -statistic degeneracy for binary  $A$  spans a frequency range approximately from  $0.9998 \times f_A$  to  $1.0002 \times f_A$ , corresponding to  $[2.090406 \times 10^{-3} \text{ Hz}, 2.091243 \times 10^{-3} \text{ Hz}]$ .

### C. The degeneracy noise of signal

Resulting from the above calculation, the  $\mathcal{F}$ -statistic for an individual source does not exhibit an isolated peak in parameter space [51, 52]. A sequence of similar elevated  $\mathcal{F}$ -statistic value emerges in the parameter space, challenging the maximum likelihood-based statistic searching algorithm, these high values of the  $\mathcal{F}$ -statistic, apart from the real binary, are termed “degeneracy noise”.

#### 1. Individual signal

We generate a singular LISA response GW signal with the parameters of binary  $A$  outlined in Tab. III. Subsequently, we introduce instrument noise to acquire mock data and compute the  $\mathcal{F}$ -statistic degeneracy for data instances with diverse parameter positions. The intentional selection of binary  $A$ , distinguished by a high SNR, aims to minimize the influence of instrument noise. In Fig. 5,

the distribution of degeneracy noise of binary  $A$  across three parameter space ( $f$ ,  $\beta$ , and  $\lambda$ ) is illustrated. Each subfigure has a spatial resolution of  $\pi/40$  radians. The colorbar indicates the  $\mathcal{F}$ -statistic value calculated at the specific parameter position. The red cross in the (2, 5) subfigure marks the real parameter position of binary  $A$ . The horizontal coordinate represents Ecliptic Longitude  $\lambda$ , while the vertical coordinate signifies Ecliptic Latitude  $\beta$ . The frequency interval between two adjacent subfigures corresponds to the minimum frequency resolution  $df = 1.59 \times 10^{-8} \text{ Hz}$  for the two-year detection. From the figure, it is evident that, in addition to the “primary peak” of the  $\mathcal{F}$ -statistic at the position of binary  $A$ , numerous “secondary peaks” with elevated  $\mathcal{F}$ -statistic values emerge. These secondary peaks represent the degeneracy noise mentioned earlier.

Fig. 6(a) and Fig. 6(b) illustrate the distribution of the  $\mathcal{F}$ -statistic in two-dimensional parameter space. The frequency resolution is  $df$ , and the Ecliptic Latitude  $\beta$  or the Ecliptic Longitude  $\lambda$  resolution is  $\pi/40$  radians. Parameters not displayed in the figures remain constant and correspond to binary  $A$ . The  $\mathcal{F}$ -statistic degeneracy in both figures (Fig. 6(a) and Fig. 6(b)) demonstrates excellent consistency with the theoretical predictions illustrated in Fig. 4(a) and Fig. 4(b).

#### 2. Two overlapped signals

Signals that overlap in parameter space introduce complexity to the distribution of the  $\mathcal{F}$ -statistic. The proximity of two signals in parameter space can lead to interference, manifesting as a high  $\mathcal{F}$ -statistic peak at an incorrect parameter position, diminishing the value at the actual binary’s parameter position. In scenarios with substantial differences in SNR between the two binaries, the impact of the low SNR signal on the high SNR signal might not be conspicuous, and the low SNR signal could be discerned by subtracting the high SNR signal. However, when overlapped signals exhibit similar SNR, their interference may yield a more pronounced  $\mathcal{F}$ -statistic peak at an incorrect parameter position. This complicates the iterative-subtraction strategy, as subtracting an incorrect waveform becomes a possibility. In our method, as long as the  $\mathcal{F}$ -statistic peak at the real binary’s parameter position does not disappear or deviate significantly, the removal of degeneracy noise, detailed in Sec. V, can effectively eliminate the erroneous  $\mathcal{F}$ -statistic peak.

Building upon binary  $A$ , we increment its frequency by integer multiples of the minimum frequency resolution  $df$  to create binary  $B$  ( $f_B = f_A + \Delta f = f_A + N \times df$ ,  $N \in \mathbb{Z}$ ). Fig. 7 illustrates the distribution of the  $\mathcal{F}$ -statistic when two signals coexist. The frequency of binary  $B$  in Fig. 7(a) and Fig. 7(b) is increased  $5 \times df$  relative to binary  $A$ , with red crosses denoting the accurate positions of both binaries—binary  $A$  on the left and binary  $B$  on the right. When the frequency difference  $\Delta f$  between two signals is  $\geq 5 \times df$ , the “primary peaks” of the

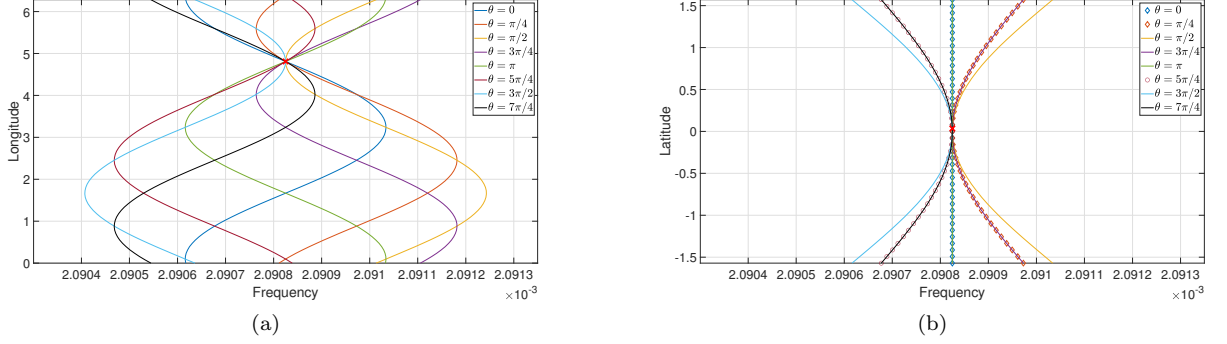


Figure 4. The  $\mathcal{F}$ -statistic degeneracy from binary  $A$  is derived according to Eq. 15. The parameters of binary  $A$ — $f_A$ ,  $\beta_A$ ,  $\lambda_A$ —are known, and the position of binary  $A$  is denoted by red cross marks. In Fig. 4(a),  $\beta'_A = \beta_A$ , and in Fig. 4(b),  $\lambda'_A = \lambda_A$ . The horizontal axis represents the frequency ( $f_{A'}$ ) of the matched waveform, binary  $A'$ , while the vertical axis represents its Ecliptic Longitude or Ecliptic Latitude ( $\lambda'_A$  or  $\beta'_A$ ).  $\theta$  denotes the angle between LISA and binary  $A$ , with different  $\theta$  values representing various positions of LISA relative to binary  $A$ .

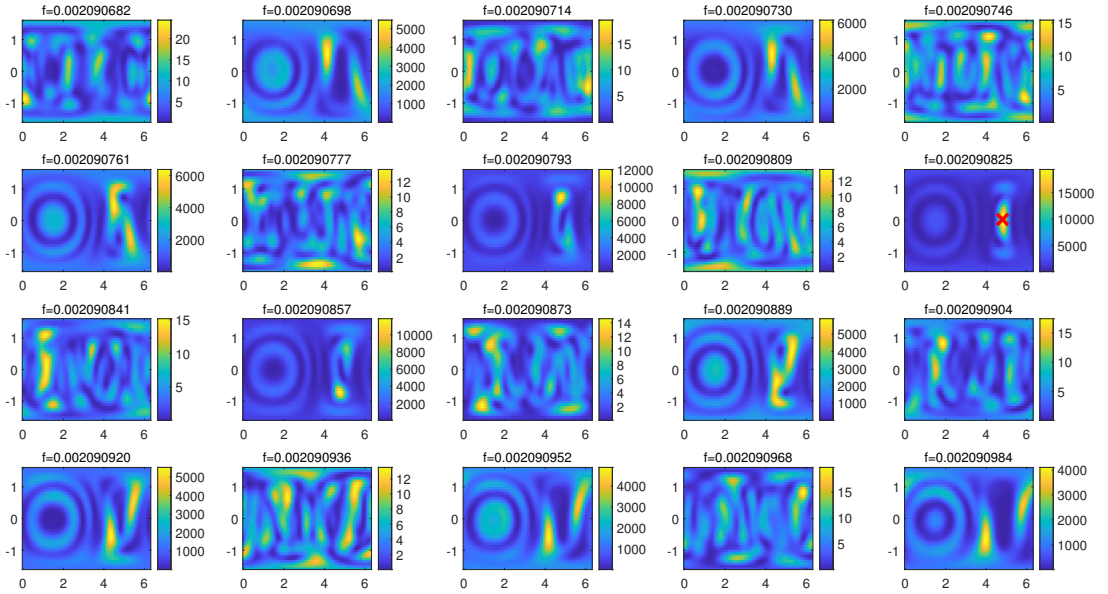


Figure 5. Slices of the  $\mathcal{F}$ -statistic in three-dimensional parameter space for binary  $A$ . The parameter position of binary  $A$  is marked in the subfigure (2, 5) with a red cross. The frequency intervals between two adjacent subfigures correspond to the minimum frequency resolution  $df = 1.59 \times 10^{-8}$  Hz. In each subfigure, the horizontal coordinate represents Ecliptic Longitude  $\lambda$ , and the vertical coordinate is Ecliptic Latitude  $\beta$ . The figure does not encompass the entire frequency range of the degeneracy noise distribution.

$\mathcal{F}$ -statistic for these two signals do not significantly influence each other, each behaving akin to a single source. However, for the binary  $B$  in Fig. 7(c) and Fig. 7(d), where the frequency of binary  $B$  is incremented by  $4 \times df$  relative to binary  $A$ , the overlap of signals causes a noticeable deviation in their  $\mathcal{F}$ -statistic behavior compared to the single signal scenario. In Fig. 7(c), two maximal  $\mathcal{F}$ -statistic peaks emerge outside the parameter positions of binaries  $A$  and  $B$ , substantially reducing the  $\mathcal{F}$ -statistic values at the true binary positions. Similarly,

in Fig. 7(d), the maximal  $\mathcal{F}$ -statistic peaks deviate from the accurate positions of the binaries. Consequently, in the iterative-subtraction method, incorrect waveforms of signals  $A$  and  $B$  would be subtracted, and the maximal  $\mathcal{F}$ -statistic peak located at a wrong parameter position for overlapped signals is referred to as “the overlapped degeneracy noise”.

When the two signals possess different SNR, the challenge posed by overlapping signals is mitigated. In Fig. 8, we adjust the amplitude  $\mathcal{A}$  of binary  $B$  to 70% of the

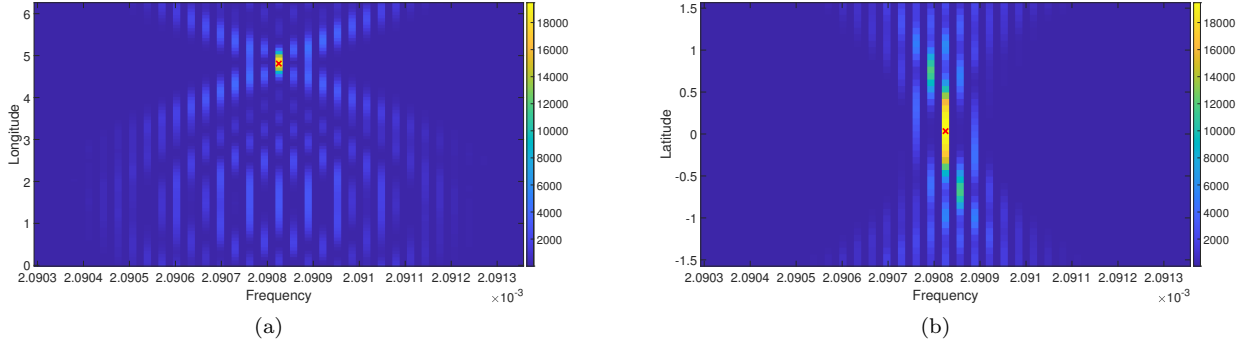


Figure 6. The red cross in the figures represent the position of binary  $A$ , while the colorbar indicate the  $\mathcal{F}$ -statistic value. The vertical coordinate corresponds to Ecliptic Longitude  $\lambda$  or Ecliptic Latitude  $\beta$ , respectively. The  $\mathcal{F}$ -statistic degeneracy for binary  $A$  spans a frequency range approximately from  $0.9998 \times f_A$  to  $1.0002 \times f_A$ , corresponding to  $[2.090406 \times 10^{-3} \text{ Hz}, 2.091243 \times 10^{-3} \text{ Hz}]$ .

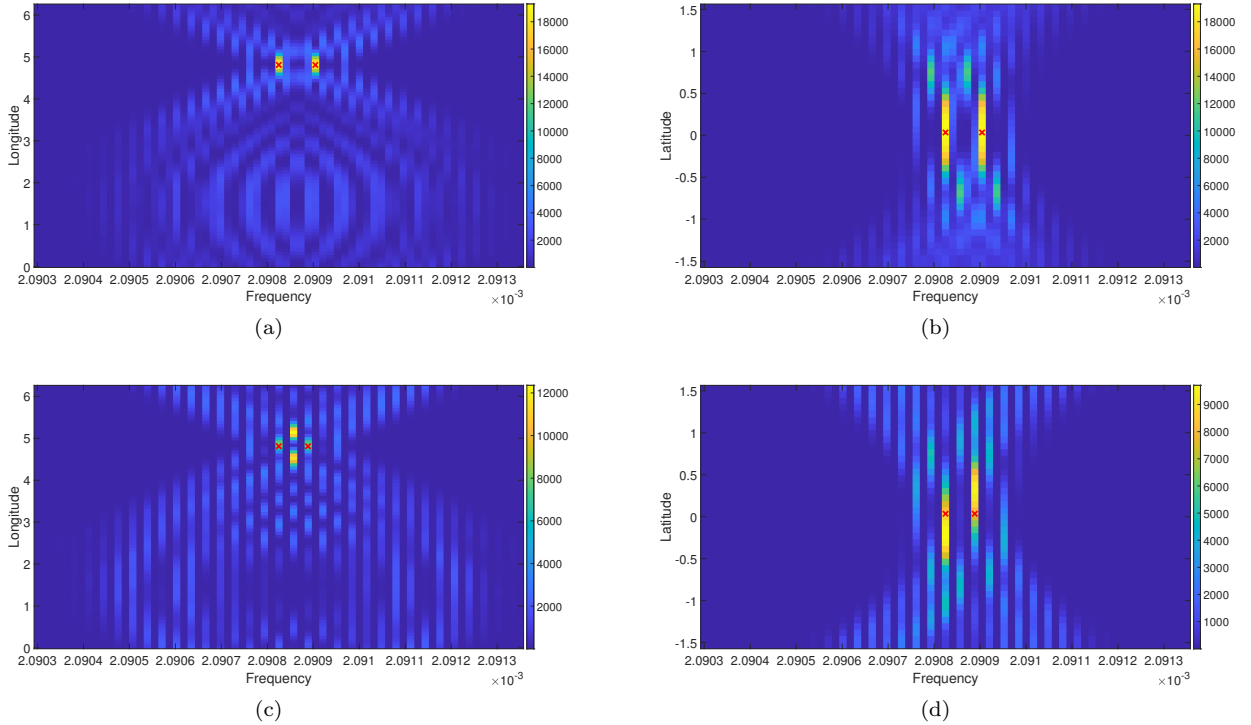


Figure 7. The  $\mathcal{F}$ -statistic degeneracy when two signals overlap. The frequency interval is  $5 \times df$  for Fig. 7(a) and Fig. 7(b), and  $4 \times df$  for Fig. 7(c) and Fig. 7(d). The red crosses marked the real positions of the two binaries.

value used in Fig. 7(c), resulting in a proportionate decrease in SNR, and the  $\mathcal{F}$ -statistic value is roughly halved. In this scenario, even though the overlapped signals continue to influence their  $\mathcal{F}$ -statistic at the two binary positions, the  $\mathcal{F}$ -statistic value of the two maximal degeneracy noise does not surpass that of binary  $A$ . Consequently, binary  $A$  maintains the maximal  $\mathcal{F}$ -statistic value in the parameter space. This situation proves advantageous for both our method and the traditional iterative-subtraction method.

We generate two new waveforms using the two wrong

maximal  $\mathcal{F}$ -statistic peaks in Fig. 7(c). The  $\mathcal{F}$ -statistic degeneracy (Fig. 9) differs from that of binary  $A$  and  $B$  in Fig. 7(c). Therefore, there is no concern that the real binaries in Fig. 7(c) will be inadvertently removed during the process of addressing degeneracy noise, as detailed in Sec. V.

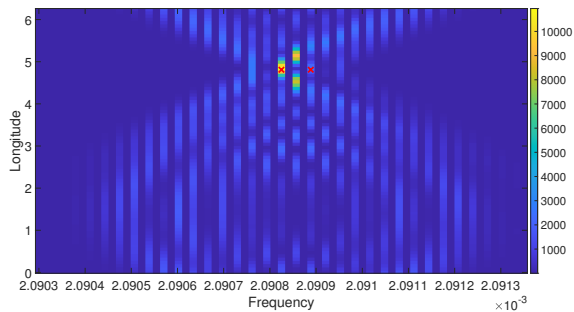


Figure 8. Binary  $A$  remains unchanged, while the amplitude  $A$  of binary  $B$  is reduced to 0.7 times its initial value, leading to a proportional decrease in SNR, and the  $\mathcal{F}$ -statistic value is approximately halved.

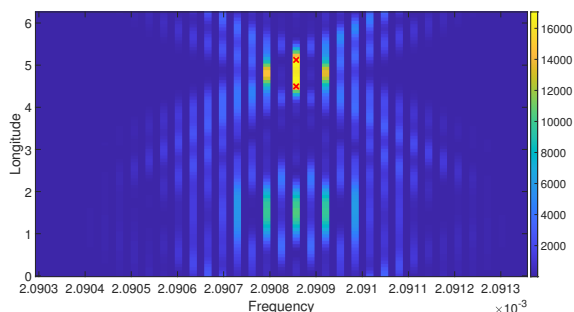


Figure 9. We generate two signals at the incorrect maximal positions of the  $\mathcal{F}$ -statistic values in Fig. 7(c) and subsequently calculate the  $\mathcal{F}$ -statistic degeneracy in the parameter space. Since the  $\mathcal{F}$ -statistic does not exhibit a high value at the positions of the two binaries in Fig. 7(c), we are not concerned that, in this scenario, removing the individual degeneracy noise in Sec. V A will inadvertently subtract the real signal from Fig. 7(c).

### 3. Three overlapped signals

It is conceivable for three or more signals with comparable SNR to overlap, especially in scenarios with low SNR and an increased number density of signals. Based on binary  $A$ , we generate two new binaries—one with a lower frequency (binary  $C$ ) and one with a higher frequency (binary  $B$ ). In Fig. 10(a) and Fig. 10(b), the frequency difference of the three signals is  $5 \times df$ , and the interference between these signals is negligible. We anticipate that separating these three signals during the search should be relatively straightforward. However, for the case where the frequency difference of these three signals is  $4 \times df$  (as shown in Fig. 10(c) and Fig. 10(d)), signal interference extinguishes the  $\mathcal{F}$ -statistic value of binary  $A$  and reduces the values of  $B$  and  $C$ . The overlapped signals also generate two erroneously prominent  $\mathcal{F}$ -statistic peaks above and below the true position of binary  $A$  (in Fig. 10(c)). This complicates the search for these three signals, and it is only possible to redis-

cover binary  $A$  after successfully disentangling binaries  $B$  and  $C$  from the data. How to search out these three overlapped signals is beyond the scope of this article.

## IV. SEARCH METHOD

### A. Data preprocessing

Before initiating the search, it is essential to preprocess the LDC1-4 data. Assuming conventional methods have detected signals with  $\text{SNR} > 15$ , our initial step involves subtracting all injected Galactic binary signals with  $\text{SNR} > 15$  from the raw data, allowing us to focus on the search for lower SNR signals. Then the data undergoes band-pass filtering and is divided into 1491 bins for parallel computation, covering a frequency range from 0.09 mHz to 15 mHz. The band-pass filter method aligns with the one illustrated in Figure 3 of Ref. [38], and other techniques, such as undersampling to reduce data length, follow the approach outlined in the same reference. As our method avoids subtracting any signal during the search, concerns about inaccurate subtraction contamination are minimized. Our primary concern shifts to addressing the potential presence of degeneracy noise at the edges of each bin. In preparation for subsequent degeneracy noise removal steps, we slightly expand the frequency search range on both sides of the acceptance zone. This extension encompasses 0.025% times outward from the boundary of the acceptance zone, ensuring coverage of all signals outside the acceptance zone whose degeneracy noise may affect the acceptance zone. This expansion is visually represented in Fig. 11.

The search ranges for  $\beta$  and  $\lambda$  cover the whole sky:  $\beta \in [-\frac{\pi}{2}, \frac{\pi}{2}]$  and  $\lambda \in [0, 2\pi]$ . The settings for  $\dot{f}$  is  $[-10^{-16}, 10^{-15}]$  when  $f \leq 4$  mHz and  $[-10^{-14}, 10^{-13}]$  when  $f > 4$  mHz.

### B. Local maxima PSO

The Particle Swarm Optimization (PSO) algorithm, renowned for its efficacy in seeking global maxima of continuous nonlinear functions [53, 54], has proven instrumental in the quest for Galactic binaries [38]. Previous methodologies focused on identifying global maxima of the  $\mathcal{F}$ -statistic within parameter space, employing multiple searches to ensure the robustness of global maxima detection. This process involved iteratively subtracting the detected signal and initiating subsequent search rounds, known as the iterative-subtraction strategy. In our LMPSO-CV approach, we streamline the process by concentrating solely on searching for local maxima, enabling us to achieve convergence with fewer steps. To facilitate this, we have tailored the PSO algorithm to swiftly converge on local maxima, optimizing the efficiency of the search process.



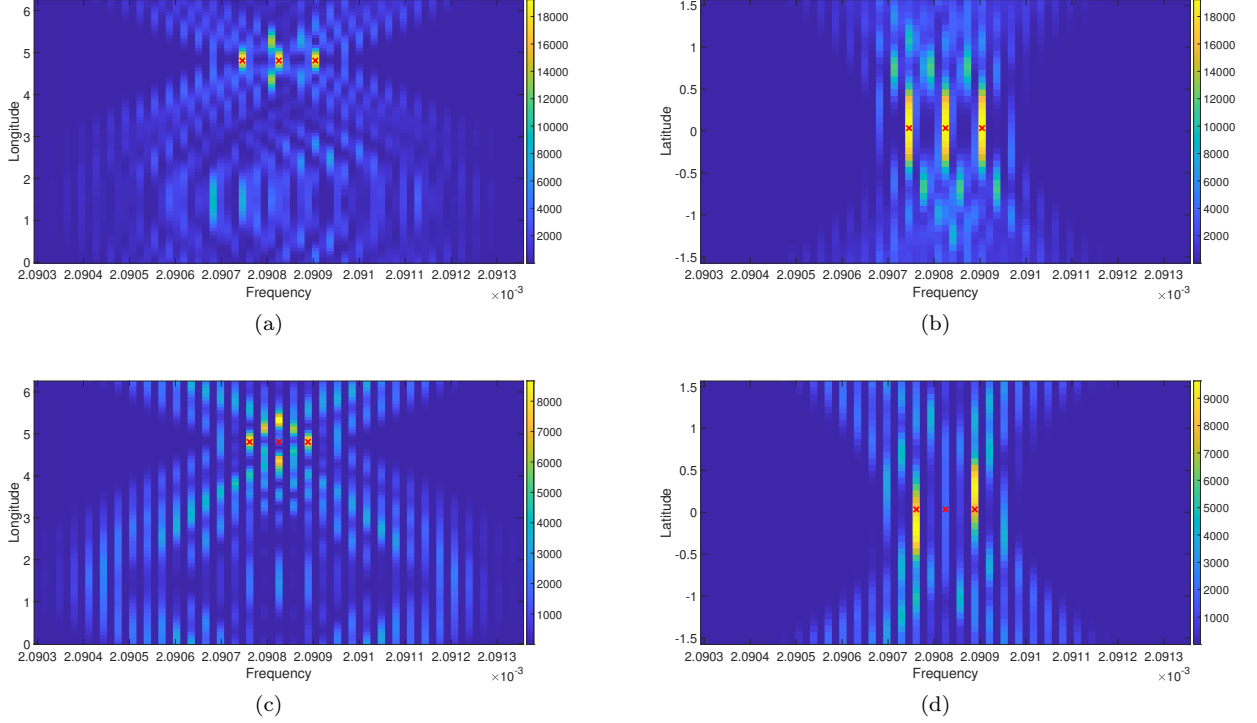


Figure 10. The  $\mathcal{F}$ -statistic degeneracy when three signals overlap. The frequency intervals are  $5 \times df$  for Fig. 10(a) and Fig. 10(b), and  $4 \times df$  for Fig. 10(c) and Fig. 10(d). The red crosses marked the positions of the three binaries.

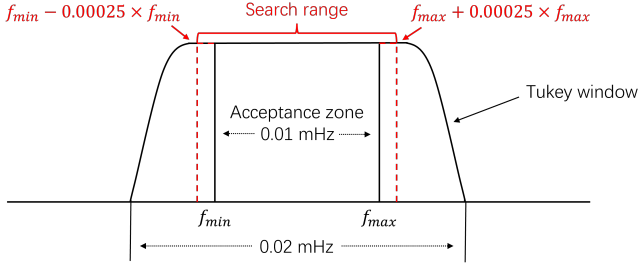


Figure 11. The schematic diagram illustrates the division of data into bins, employing a method similar to that outlined in Ref. [38]. However, it is crucial to note that our approach does not involve searching the entire range of each bin. Instead, our focus is directed towards exploring the specific range within each bin where signals may generate degeneracy noise within the acceptance zone.

We employ a total of 40 particles in our algorithm. The process begins by randomly dispersing these particles throughout the parameter space. Each particle calculates the  $\mathcal{F}$ -statistic value at its respective position. Based on the calculation results, the positions of the particles undergo iteration. Each particle “remembers” the best value and the position it explored, denoted as the personal best position ( $P$ ). From the  $P$  of all particles, the global best position ( $G$ ) is determined to represent the globally best position found by the swarm. To reach

the optimal solution, each particle moves toward both its  $P$  and the  $G$  within the swarm. The position of each particle is updated in each iteration through the following equation:

$$\begin{aligned} \mathbf{v}_i^{t+1} &= \omega \mathbf{v}_i^t + c_1 \mathbf{r}_1 \cdot (P_i^t - \mathbf{x}_i^t) + c_2 \mathbf{r}_2 \cdot (G^t - \mathbf{x}_i^t), \\ \mathbf{x}_i^{t+1} &= \mathbf{x}_i^t + \mathbf{v}_i^{t+1}. \end{aligned} \quad (18)$$

In the given equation,  $t$  denotes the number of iterations.  $\mathbf{v}$  represents the velocity vector.  $\omega$  serves as the inertia weight crucial for balancing local exploitation and global exploration.  $\mathbf{r}_1$  and  $\mathbf{r}_2$  denote random vectors uniformly distributed within the range  $[0, 1]^D$  ( $D$  is the dimensionality of the searched parameter space).  $\mathbf{x}_i$  indicates the position of the  $i$ -th particle.  $c_1$  and  $c_2$ , referred to as “acceleration coefficients”, are positive constants. In particular, when  $c_1 = c_2 = 2$  and  $\omega = \max(\omega_1 - \frac{\omega_2 t}{\omega_3}, \omega_4)$  (where  $\omega_1 = 0.9$ ,  $\omega_2 = 0.4$ ,  $\omega_3 = 1999$ ,  $\omega_4 = 0.2$ ), this parameter configuration strikes a harmonious balance between  $P$  and  $G$ , rendering the PSO algorithm highly effective in the pursuit of the global maxima.

In the employed PSO algorithm, we initially configure the parameters as described above. Upon reaching an optimal  $\mathcal{F}$ -statistic surpassing a predefined threshold ( $\mathcal{F}$ -statistic  $> 53$ , corresponding to  $\text{SNR} > 7$ ), we dynamically adjust the parameter configuration by setting  $c_1 = \omega = 0$  in the iterative equation. So the iterative

equation becomes:

$$\begin{aligned} \mathbf{v}_i^{t+1} &= c_2 \mathbf{r}_2 \cdot (\mathbf{G}^t - \mathbf{x}_i^t), \\ \mathbf{x}_i^{t+1} &= \mathbf{x}_i^t + \mathbf{v}_i^{t+1}. \end{aligned} \quad (19)$$

This adjustment accelerates the convergence of the PSO algorithm towards a local maxima. To ascertain convergence, we implement an automatic convergence criterion: if the optimal  $\mathcal{F}$ -statistic value remains constant for 15 consecutive iterations, convergence is determined, and facilitating the transition to search the next local maxima.

The flow chart of LMPSO in Fig. 14 illustrates the workflow of the LMPSO algorithm. Following the completion of each local maxima search, we create a void in the parameter space corresponding to the position of the  $G$ . In the subsequent search, particles are initially assessed to determine if they fall within the voids. If a particle lands in the voids, its value is assigned negative infinity, indicating that the particle is invalid. For the algorithm, this signifies a position that requires no further exploration. During the next iteration, the particle will navigate to other positions in the parameter space. As the maximum  $\mathcal{F}$ -statistic value surpasses a predefined threshold ( $\mathcal{F}$ -statistic  $> 53$ ), the search transitions from global to local maxima. Ultimately, the convergence criterion adjudicates whether the search is concluded.

### C. Create voids in the parameter space

After identifying a local maxima using LMPSO algorithm, we create a void in the parameter space to prevent redundant searches. The void is modeled as a spheroid described by the ellipsoid equation ( $\frac{x^2}{a^2} + \frac{y^2}{b^2} + \frac{z^2}{c^2} = 1$ ), where  $a$ ,  $b$ , and  $c$  represent the radii of the spheroid in  $f$ ,  $\beta$ , and  $\lambda$ , respectively. We set  $a = df$  to be equal to the minimum frequency resolution. The values for  $b$  and  $c$  depend on the  $\mathcal{F}$ -statistic degeneracy calculated in Fig. 12. In this figure, while keeping the other parameters constant, we vary one parameter at a time to observe the trend of the  $\mathcal{F}$ -statistic in  $\beta$  or  $\lambda$ . Specifically, Fig. 12(a) explores the variation with respect to  $\beta$ , and Fig. 12(b) with respect to  $\lambda$ . The resolution of  $\beta$  and  $\lambda$  is  $\pi/40$  radian. We determine the ellipsoidal radius by selecting half the distance between the two local minima closest to the searched local maxima. The positions of these two local minima are denoted by the left boundary and right boundary lines in Fig. 12(a) and Fig. 12(b), with the red cross marking the real binary position.

In the subsequent search, we must assess whether the particles in the LMPSO fall within the voids. This is determined using the formula

$$D = \frac{(x_1 - x)^2}{a^2} + \frac{(y_1 - y)^2}{b^2} + \frac{(z_1 - z)^2}{c^2} \quad (20)$$

where  $x_1$ ,  $y_1$ ,  $z_1$  represent the three parameter positions of the particle, and  $x$ ,  $y$ ,  $z$  represent the searched local maxima position at the center of the void. When  $D > 1$ ,

it indicates that the particle is outside the void, and we proceed to calculate the  $\mathcal{F}$ -statistic value of the particle. Conversely, when  $D \leq 1$ , it indicates that the particle is inside the void, and we assign it an infinity value, rendering it an invalid particle. It will be repositioned elsewhere in the subsequent iteration. Fig. 13 illustrates the voids in normalized parameter space. The vertical coordinates in Fig. 13(a) represent  $\beta$ , while Fig. 13(b) represents  $\lambda$ . Notably, the radius of the void at latitude is larger than that at longitude, suggesting that the  $\mathcal{F}$ -statistic is more sensitive to longitude. Although the radius in frequency is set at  $df$ , for clarity in the figure, we use  $6 \times df$  as an example.

Ultimately, we have generated numerous “voids” in the parameter space, each indicating the presence of a local maxima. The count of local maxima far surpasses the number of binaries. In Sec. V, we will conduct an analysis of these voids, which we call find-real- $\mathcal{F}$ -statistic-analysis, to identify real binaries and eliminate noise.

### D. Termination rule of search

The criterion for concluding the search can greatly impact the number of voids. We conducted a maximum of 10,000 searches per bin. Alternatively, if the  $\mathcal{F}$ -statistic values remain below the threshold ( $\mathcal{F}$ -statistic = 53) for 30 consecutive searches (equivalent to 30 consecutive local maxima), the search is terminated. Ultimately, none of the bins met the first criterion. The frequency range with the highest number of searched local maxima is from 2.305 mHz to 2.315 mHz, resulting in 3206 voids.

## V. FIND-REAL- $\mathcal{F}$ -STATISTIC-ANALYSIS

Given the existence of degeneracy noise, the count of local maxima far exceeds the number of real binaries, a situation exacerbated by the influence of instrument noise. Without effective noise removal, the search outcomes become severely contaminated. In this section, our primary goal is the removal of both degeneracy noise and instrument noise, striving to achieve the most accurate representation of the search results. We term this comprehensive analysis “find-real- $\mathcal{F}$ -statistic-analysis”.

### A. Remove individual signal degeneracy noise

The degeneracy noise produced by an individual signal is the most numerous and easiest to remove, characterized by relatively weaker  $\mathcal{F}$ -statistic values compared to the binaries from which they originate, so we commence by systematically eliminating individual signal degeneracy noise. The starting point for this removal process is the descending list of searched local maxima, ordered by their  $\mathcal{F}$ -statistic values. Beginning with the local maxima

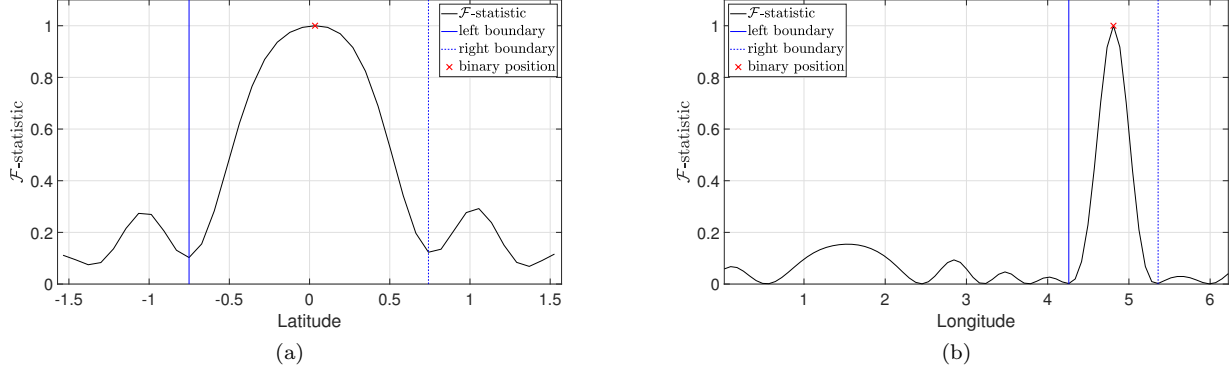


Figure 12. We conduct an analysis of the normalized  $\mathcal{F}$ -statistic degeneracy to determine the void radii within the Ecliptic Latitude  $\beta$  and Ecliptic Longitude  $\lambda$ . Throughout this computation, all other parameters are kept constant while one parameter is systematically varied at a time. Specifically, in Fig. 12(a), we investigate the effects of changing  $\beta$ , and in Fig. 12(b), we explore the impact of varying  $\lambda$ . The spatial resolution employed is  $\pi/40$  radians. The determination of the ellipsoidal radius associated with each parameter involves selecting half the distance between the two local minima, identified by the left boundary and right boundary, which are closest to the sought local maxima. The position of the sought local maxima is denoted by the red cross, symbolizing the authentic binary position in our analysis.

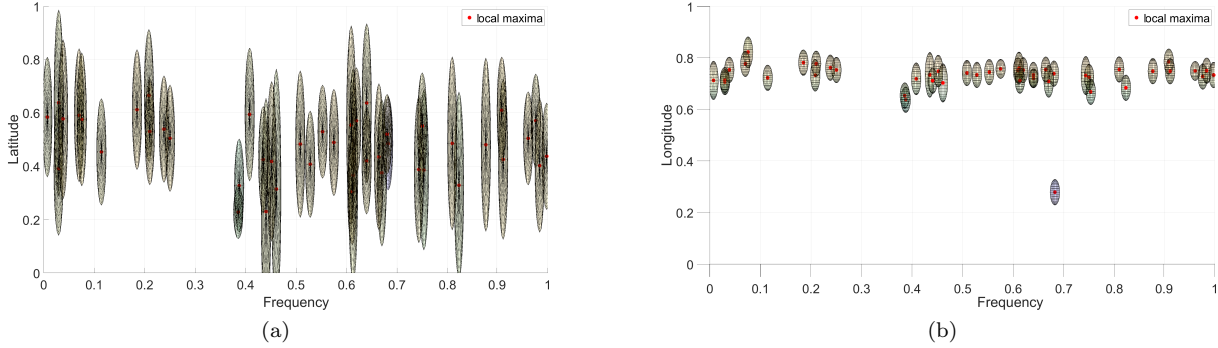


Figure 13. The example for the voids in normalized parameter space. Fig. 13(a) and Fig. 13(b) are the two side views. The red points represent the local maxima inside each void. To make the example more obvious, we take the radius on frequency  $6 \times df$  in the figures rather than  $1 \times df$  in real search.

possessing the highest  $\mathcal{F}$ -statistic value, indicative of potential authenticity as a real binary, we generate its LISA response GW signal as the initial waveform. Having obtained the initial waveform, we proceed to scrutinize the second-largest  $\mathcal{F}$ -statistic value to ascertain whether it corresponds to the degeneracy noise of the first. This involves computing the  $\mathcal{F}$ -statistic value using the parameters of the second local maxima on the first waveform. Subsequently, we deduct the computed  $\mathcal{F}$ -statistic value of the second local maxima on the first waveform from its own searched  $\mathcal{F}$ -statistic value. If the difference exceeds the threshold ( $\Delta\mathcal{F}\text{-statistic} > 53$ ), it is considered a new signal to retain. We then generate its waveform and incorporate it into the first waveform. Conversely, if the difference falls below the threshold, it is identified as noise and promptly removed. The formula for computing

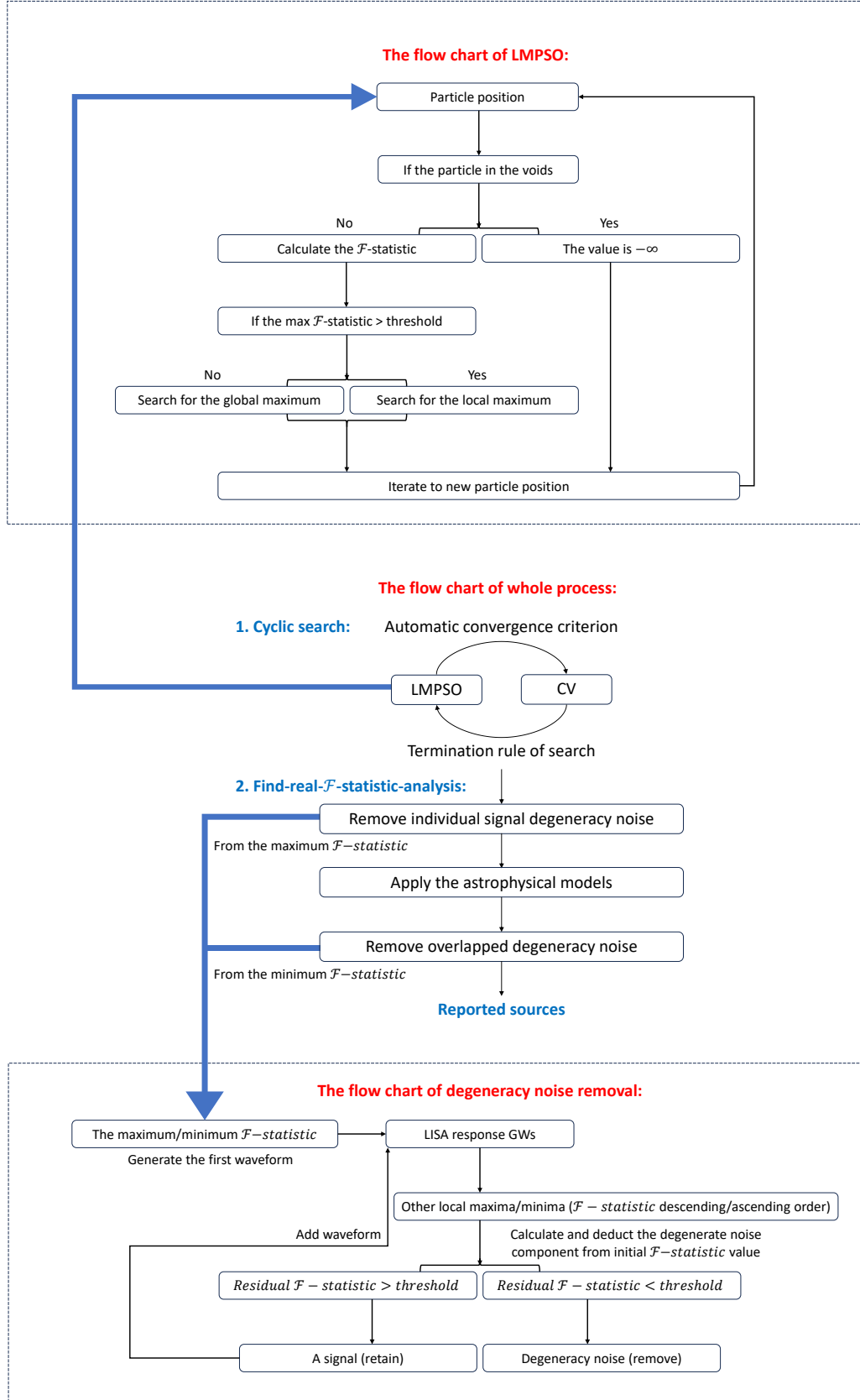
the  $\Delta\mathcal{F}$ -statistic is given by:

$$\Delta\mathcal{F}(\theta_i) = \mathcal{F}(\theta_i, S) - \mathcal{F}\left(\theta_i, \sum_{m=1}^{i-1} h(\theta_m)\right), \quad (21)$$

where  $S$  represents the raw data, specifically the LDC1-4 residual data in this article. The term  $\mathcal{F}(\theta_i, S)$  denotes the  $\mathcal{F}$ -statistic value for  $i$  local maxima with parameters  $\theta_i$  concerning the data  $S$  (the searched  $\mathcal{F}$ -statistic value). Similarly,  $\mathcal{F}\left(\theta_i, \sum_{m=1}^{i-1} h(\theta_m)\right)$  represents the  $\mathcal{F}$ -statistic value for  $i$  local maxima concerning the sum of the first  $i - 1$  retained waveforms (the computed  $\mathcal{F}$ -statistic value).

This iterative procedure continues, processing all local maxima in descending order of  $\mathcal{F}$ -statistic. Ultimately, this step significantly reduces the number of initially searched local maxima from the total count of 646,120 (646,120 with  $\mathcal{F}$ -statistic  $> 53$ , and the overall total is

Figure 14. The flow chart of our method.



849,576) to 25,615, which are the ones remaining within the acceptance zone after the removal of individual signal degeneracy noise. The flow chart of degeneracy noise removal in Fig. 14 visually outlines the process.

## B. Apply the astrophysical models

With diminishing SNR, the influence of instrument and confusion noise becomes increasingly conspicuous. Identifying instrument noise false alarm in one search is challenging. In order to mitigate the effects of instrument noise, we undertake a secondary search by fine-tuning the  $\dot{f}$  parameter setting. Subsequently, we cross-validate the outcomes derived from the two distinct searches, thereby proficiently eliminating the impact of instrument noise from the dataset.

### 1. The second search based on astrophysical models

In the subsequent search, we maintain the configurations for all other parameters while specifically adjusting the range for  $\dot{f}$ . In the initial search, we provided an extensive range for  $\dot{f}$ , encompassing  $[-10^{-16}, 10^{-15}]$  when  $f \leq 4$  mHz and  $[-10^{-14}, 10^{-13}]$  when  $f > 4$  mHz. For the second search, we apply the astrophysical model to restrict the  $\dot{f}$  range for each frequency bin, employing a logarithmic scale of 10 for the search. The  $\dot{f}$  range for Galactic binaries can be determined using the astrophysical model:

$$\dot{f} = \frac{96}{5} \pi^{8/3} \mathcal{M}^{5/3} f^{11/3}. \quad (22)$$

Considering that the majority of Galactic binaries involve white dwarfs with masses ranging from  $0.1 M_{\odot}$  [55] to  $1.4 M_{\odot}$ , we determine the range of the chirp mass  $\mathcal{M} = (m_1 m_2)^{3/5} / M^{1/5}$ . Here,  $m_1$  and  $m_2$  represent the masses of the two white dwarfs, and  $M = m_1 + m_2$  denotes their total mass. The lower and upper limits of the chirp mass  $\mathcal{M}$  are  $\mathcal{M}_{\min} = 0.06 M_{\odot}$  and  $\mathcal{M}_{\max} = 1.22 M_{\odot}$ , respectively. In contrast to the first search, the  $\dot{f}$  range for the second search is constrained to a narrower interval, with its magnitude being proportional to the frequency.

### 2. Cross validation

In the second search, a substantial number of local maxima are identified, totaling 574,676 with  $\mathcal{F}$ -statistic  $> 53$  (out of a total of 822,730). Following the removal of individual degeneracy noise, 26,759 local maxima within the acceptance zone are retained. To evaluate the similarity between the gravitational waveforms of the two searches, we calculate the correlation coefficient  $R_{ee}$  (Eq. 23) between the 25,615 local maxima from the first search and the 26,759 local maxima from the second

search. Local maxima with  $R_{ee} > 0.99$  in the first search are considered more reliable, resulting in the selection of 10,623 local maxima for the subsequent step. This may be attributed to the heightened sensitivity of instrument noise to  $\dot{f}$  when imitating a signal, whereas real signals demonstrate greater robustness to variations in  $\dot{f}$ .

### 3. Restrict the Galactic Latitude

The distribution of degeneracy noise spans the entire celestial sphere. However, leveraging the well-established concentration of Galactic binaries in the Galactic Disk, we can enhance the precision of the search results by introducing constraints on their sky locations. By confining the Galactic Latitude of the outcomes within the range of  $-0.5$  rad to  $0.5$  rad (as illustrated in Fig. 1), we effectively narrow down the selection to 9,143 remaining local maxima.

## C. Remove overlapped signals degeneracy noise

In the final phase, our aim is to eliminate the overlapped degeneracy noise originating from the simultaneous presence of two or more binaries (as depicted in Fig. 7(c)). Since the  $\mathcal{F}$ -statistic value of such noise exceeds that of any individual binary it emanates from, it cannot be effectively addressed in the initial step designed to remove individual signal degeneracy noise. To tackle these instances of overlapped degeneracy noise, we repeat the first step in ascending order of the searched local maxima, as illustrated in the flow chart of degeneracy noise removal depicted in Fig. 14. The waveform is initially generated by the signal with the lowest  $\mathcal{F}$ -statistic value and progressively incorporates signals with higher  $\mathcal{F}$ -statistic value. The objective is to discern whether the signal with the higher  $\mathcal{F}$ -statistic value is degeneracy noise resulting from overlapping with signals with lower  $\mathcal{F}$ -statistic values.

Following this step, 8,995 local maxima persist.

## VI. SEARCH RESULTS

To determine the accuracy of the searched sources, we need to calculate the correlation coefficient ( $R$ ) of the results with the injection sources:

$$R(\theta, \theta') = \frac{C(\theta, \theta')}{[C(\theta, \theta)C(\theta', \theta')]^{1/2}}, \quad (23)$$

$$C(\theta, \theta') = \sum_I (\bar{s}^I(\theta) * \bar{s}^I(\theta')) / S_n^I(f),$$

where  $\theta$  and  $\theta'$  represent the parameters, and  $I \in \{A, E, T\}$ . We selected injection sources with  $3 < \text{SNR} < 15$  over a two-year observation period for calculation,



with a total count of 55,714. A source is considered accurate if its  $R \geq 0.9$ , relatively accurate if  $0.8 \leq R < 0.9$ , and contaminated if  $0.5 \leq R < 0.8$ .

### A. Detection rate and SNR

We employ the reported sources to represent the outcomes following the find-real- $\mathcal{F}$ -statistic-analysis, and confirmed sources to signify those reported sources with an  $R$  value exceeding the threshold  $R_t$ . The detection rate (DR) is succinctly formulated by their numbers as follows:

$$\text{DR} = \frac{N_c}{N_r}, \quad (24)$$

where  $N_r$  is the number of reported sources, and  $N_c$  is the number of confirmed sources. The evolutionary trajectory of our methodology through the various stages of find-real- $\mathcal{F}$ -statistic-analysis (elaborated in Sec. V) is vividly depicted in the histogram of  $R$  presented in Fig. 15. In the initial step, a significant reduction in individual degeneracy noise was achieved, resulting in 25,615 reported sources with a DR of 23.2% at  $R_t = 0.8$  (A). The second step concentrated on diminishing instrument noise through cross-validation with a secondary search, yielding 10,623 reported sources and a DR of 45.2% at  $R_t = 0.8$  (B2). Subsequent refinement in the third step, which confined Galactic Latitude within  $\pm 0.5$  rad, led to a reduction to 9,143 reported sources and a DR of 52.0% at  $R_t = 0.8$  (B3). Finally, the fourth step addressed overlapped degeneracy noise with  $\mathcal{F}$ -statistic values surpassing those of any individual signal, resulting in 8,995 reported sources and a DR of 52.3% at  $R_t = 0.8$  (C).

In Fig. 15, the designation “D” characterizes the capability to identify reliable sources based on the variation in  $\mathcal{F}$ -statistic values before and after the find-real- $\mathcal{F}$ -statistic-analysis. Specifically, we select sources for which the  $\mathcal{F}$ -statistic value demonstrates a change of less than 10% before and after the find-real- $\mathcal{F}$ -statistic-analysis, resulting in a DR of 73.1% (D). However, it is crucial to note that this method is effective mainly for selecting more isolated sources unaffected by other signals. Consequently, the number of reported sources decreases to 3,463. Therefore, we do not consider this approach as an integral part of the find-real- $\mathcal{F}$ -statistic-analysis. In the subsequent sections of the article, we exclusively present the reported sources obtained through the find-real- $\mathcal{F}$ -statistic-analysis, rather than the “D” result with a higher detection rate.

Owing to signal overlap, the  $\mathcal{F}$ -statistic value for each source may receive contributions from other sources, resulting in an inflated SNR. To illustrate this effect, we depict the SNR-ratio between confirmed sources ( $R_t = 0.8$ ) and their corresponding injection sources in Fig. 16.

$$\text{SNR-ratio} = \frac{\text{SNR}_{\text{con}}}{\text{SNR}_{\text{inj}}}. \quad (25)$$

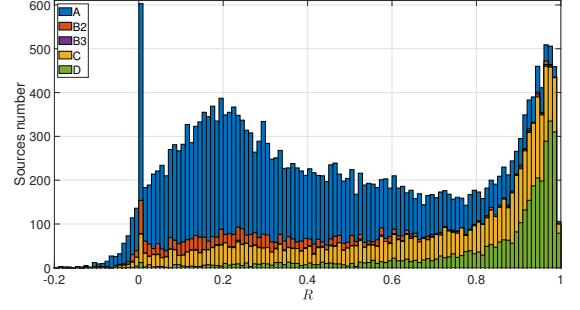


Figure 15. The histogram depicts the distribution of correlation coefficients in the results after each step. A, B2, B3, and C correspond to the four steps outlined in Sec. V. A signifies the outcomes after eliminating individual signal degeneracy noise (Sec. V A). B2 represents the results after cross-validation with the second search (Sec. V B2). B3 indicates the outcomes after restricting the Galactic Latitude (Sec. V B3), and C denotes the reported sources after removing overlapped degeneracy noise (Sec. V C). D designates the sources for which the change in  $\mathcal{F}$ -statistic value is less than 10% before and after the identification of the real  $\mathcal{F}$ -statistic analysis.

The sources are arranged in ascending frequency order, and to achieve a smoother curve, we take an average for every 50 sources. In Fig. 16, “unremove degeneracy noise” refers to the SNR before the find-real- $\mathcal{F}$ -statistic analysis, while “remove degeneracy noise” corresponds to the SNR after the find-real- $\mathcal{F}$ -statistic analysis (the steps for removing degeneracy noise are outlined in Sec. V A and Sec. V C). The average SNR-ratio is 1.22 and 1.10 for “unremove degeneracy noise” and “remove degeneracy noise”, respectively. After the find-real- $\mathcal{F}$ -statistic analysis, the fact that the average SNR-ratio approaches 1 indicates a closer match between the SNR of the confirmed sources and their corresponding injection sources, as the  $\mathcal{F}$ -statistic component from other sources has been eliminated. As the frequency increases, the SNR-ratio gradually converges to 1. However, at lower frequencies ( $f < 2 \times 10^{-3}$  Hz), a substantial number of unresolved Galactic binaries contribute energy (degeneracy noise) to the confirmed sources, leading to  $\text{SNR}_{\text{con}}$  being significantly larger than their corresponding  $\text{SNR}_{\text{inj}}$ .

The distribution of reported sources in different SNR and  $R$  ranges is illustrated in Fig. 17. Each cell on SNR has a width of 2, and on  $R$ , it is 0.01. The highest density of the distribution is in the range where  $R$  spans from 0.98 to 0.99, and SNR from 13 to 15, as well as in the range where  $R$  ranges from 0.97 to 0.98, and SNR from 11 to 13. Some reported sources have  $\text{SNR} > 15$ , which may be influenced by instrument noise and overlapped signals.

The DR is also sensitive to the SNR of the sources. We put the number of these sources in different conditions and the associated DR in Tab. I. For the reported sources (C), the lowest DR occurs when the SNR range

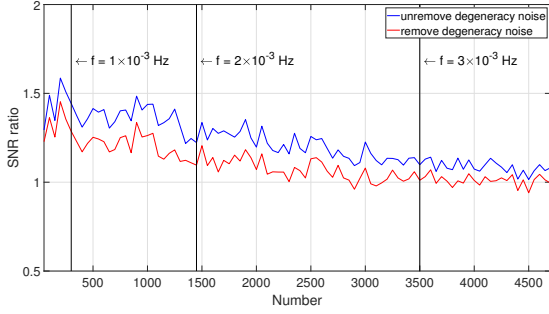


Figure 16. The SNR-ratio is calculated for confirmed sources ( $R_t = 0.8$ ) in comparison to their corresponding injection sources. The term “unremove degeneracy noise” signifies the SNR before the find-real- $\mathcal{F}$ -statistic analysis, whereas “remove degeneracy noise” indicates the SNR after the find-real- $\mathcal{F}$ -statistic analysis.

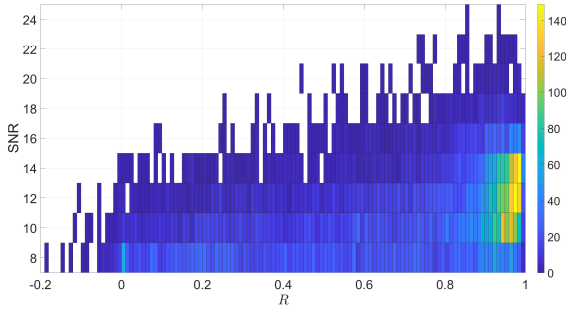


Figure 17. The distribution of reported sources in different SNR and  $R$  ranges.

is between  $7 \sim 9$ , and  $R_t = 0.9$ . Due to the lower SNR of these signals, they deviate more from the parameter position of the binary, exhibiting higher sensitivity to noise. The highest DR occurs when  $\text{SNR} > 13$  and  $R_t = 0.5$ . The higher SNR and lower  $R$  threshold result in  $\text{DR} = 94.0\%$ . In conclusion, the DR reduced with the decrease of SNR and the increase of  $R_t$ .

## B. Compared with other method

There have been recent developments in the search for LDC1-4 data [38, 43, 44]. As our focus primarily lies on sources with injection sources’  $\text{SNR} < 15$ , direct comparison with their findings is not feasible. However, by referring to Table I in Ref. [38], we can make a rough assessment of the effectiveness of our methods. They present the main outcomes of their method applied to the LDC1-4 data, categorizing sources’ frequencies into three distinct regions. Similarly, we categorize our results into the same three regions, as shown in Tab. II. The Ref. [38] has 2778 reported sources with  $f < 3$  mHz and  $\text{SNR} < 25$ . Since there are approximately 3000 injection sources within the SNR range of  $15 \sim 25$  and

$f < 3$  mHz, it appears that Ref. [38] might not have extensively searched for sources with  $f < 3$  mHz and  $\text{SNR} < 15$ . Conversely, our method identifies 7399 reported sources within the range, exhibiting varying performance depending on the chosen  $R_t$ . Hence, our approach may perform better in the low frequency and low SNR range. A similar comparison can be drawn for the region  $3 \text{ mHz} < f < 4 \text{ mHz}$ . The Ref. [38] has 1629 reported sources with  $3 \text{ mHz} < f < 4 \text{ mHz}$  and  $\text{SNR} < 20$ , while approximately 800 injection sources fall within the SNR range of  $15 \sim 20$  in the same frequency band. This suggests that there may be around 800 reported sources in Ref. [38] with  $3 \text{ mHz} < f < 4 \text{ mHz}$  and  $\text{SNR} < 15$ . However, our search reveals 1590 reported sources within this range. Even accounting for the differences in the detection rate, we accurately identified more confirmed sources. For  $f > 4$  mHz, there are approximately 1000 injection sources with  $\text{SNR} < 15$ , where our method does not perform as effectively as that of Ref. [38]. We provide an explanation for this discrepancy in Sec. VI E. Overall, our approach demonstrates a comparative advantage in low frequency and low SNR regions.

Indeed, the number of confirmed sources searched in Ref. [38] and the injection sources eliminated by us to acquire the LDC1-4 residual data are comparable. According to our hypothesis, we can first employ the Ref. [38] or other methods to identify sources with high SNR or high frequency and subsequently utilize our method to detect those with low SNR and low frequency in the residual. Given the higher density of low SNR sources, the overlap among them will exceed that of high SNR sources (as shown in Appendix B). The Ref. [38] method risks subtracting “secondary peaks”, which will lead to the energy loss of real signal and potentially affect the position of the “primary peak”. In contrast, our method entails identifying all peaks without subtraction, followed by retaining the “primary peak” and discarding the “secondary peaks”. This strategy avoids the effect of inaccurate subtraction contamination.

Our pipeline can also be applied to high SNR sources (e.g.,  $\text{SNR} \geq 15$ ), but the significant amount of degeneracy noise originating from high SNR sources will impose greater demands on computing resources. Therefore, we believe it is preferable to initially employ the Ref. [38] or other methods to process high SNR sources and subsequently utilize our pipeline to search for low SNR sources in the residual data. Our pipeline is primarily designed for scenarios where numerous sources with similar SNR coexist, making it particularly effective for detecting low SNR and low-frequency sources.

## C. Parameter errors

When we taking different  $R_t$ , the reported sources exhibit varying parameter errors. We categorize the reported sources into three groups based on  $R$ :  $R \geq 0.9$ ,  $0.8 \leq R < 0.9$ , and  $0.5 \leq R < 0.8$ , and investigate the mag-

	SNR	7 ~ 9	9 ~ 11	11 ~ 13	> 13	All
C	$N_r$	2554	2412	1942	2087	8995
	DR ( $R_t = 0.5$ )	52.5%	74.5%	85.5%	94.0%	75.2%
	DR ( $R_t = 0.8$ )	25.6%	49.7%	62.8%	78.2%	52.3%
	DR ( $R_t = 0.9$ )	14.5%	33.4%	47.1%	59.2%	36.9%
D	$N_r$	177	744	1031	1511	3463
	DR ( $R_t = 0.5$ )	59.3%	82.7%	90.4%	96.3%	89.7%
	DR ( $R_t = 0.8$ )	42.4%	66.0%	71.2%	81.4%	73.1%
	DR ( $R_t = 0.9$ )	28.2%	50.3%	58.1%	64.1%	57.5%
	Frequency	$1 \times 10^{-4} \text{ Hz} \sim 1.5 \times 10^{-2} \text{ Hz}$				

Table I. The number and detection rate of reported sources (C) and the D results in Fig. 15, when we take different  $R_t$  and ranges of SNR. Our objective is to identify sources with SNR > 7 in the LDC1-4 residual data, from which all injection sources with SNR  $\geq 15$  have been eliminated. However, due to noise effects, some reported sources exhibit SNR > 15, as illustrated in Fig. 16 and Fig. 17.

	Frequency	< 3 mHz	3 ~ 4 mHz	> 4 mHz	All
C	$N_r$	7399	1590	6	8995
	DR ( $R_t = 0.5$ )	72.0%	89.9%	83.3%	75.2%
	DR ( $R_t = 0.8$ )	47.2%	75.8%	66.7%	52.3%
	DR ( $R_t = 0.9$ )	30.6%	66.3%	66.7%	36.9%
D	$N_r$	2626	832	5	3463
	DR ( $R_t = 0.5$ )	86.7%	99.0%	100.0%	89.7%
	DR ( $R_t = 0.8$ )	66.2%	94.7%	80.0%	73.1%
	DR ( $R_t = 0.9$ )	47.9%	87.9%	80.0%	57.5%
	Injection sources' SNR	3 ~ 15			

Table II. The number and detection rate of reported sources (C) and the D results in Fig. 15, when we take different  $R_t$  and ranges of frequency. We utilize injection sources with SNR ranging from 3 to 15 to compute the correlation coefficient, ensuring that our confirmed sources fall within this range and do not correspond to injection sources with higher SNR.

nitude of parameter errors for each category in Fig. 18. For sources with  $R \geq 0.9$ , characterized by high correlation coefficients, the parameter errors are relatively lower. Their average errors in  $f$ ,  $\dot{f}$ ,  $\beta$ , and  $\lambda$  are  $3.11 \times 10^{-9}$  Hz,  $9.42 \times 10^{-17}$  Hz<sup>2</sup>, 0.07 rad, and 0.03 rad, respectively. In the case of sources with  $0.8 \leq R < 0.9$ , the average errors in  $f$ ,  $\dot{f}$ ,  $\beta$ , and  $\lambda$  are  $3.85 \times 10^{-9}$  Hz,  $1.10 \times 10^{-16}$  Hz<sup>2</sup>, 0.13 rad, and 0.08 rad, respectively. For sources with  $0.5 \leq R < 0.8$ , characterized by low correlation coefficients, the parameter errors are higher. Their average errors in  $f$ ,  $\dot{f}$ ,  $\beta$ , and  $\lambda$  are  $2.16 \times 10^{-8}$  Hz,  $1.22 \times 10^{-16}$  Hz<sup>2</sup>, 0.31 rad, and 0.28 rad, respectively. The secondary peaks on either side of the main peak of  $\Delta f$  in Fig. 18 for sources with  $0.5 \leq R < 0.8$  suggest that some sources, whose  $f$  values deviate from those of the real binary by an amount greater than the minimum frequency resolution  $df = 1.59 \times 10^{-8}$  Hz for the two-year detection, have been searched in the degeneracy noise position.

For sources with  $0.8 \leq R < 0.9$ , the rate of change in the average errors of  $f$ ,  $\dot{f}$ ,  $\beta$ , and  $\lambda$  parameters, relative to sources with  $R \geq 0.9$ , are 23.8%, 16.8%, 85.7%, and 166.7%, respectively. Therefore, the main difference between relatively accurate sources and accurate sources lies in the accuracy of the sky position. For sources with  $0.5 \leq R < 0.8$ , the rate of change in the average errors of  $f$ ,  $\dot{f}$ ,  $\beta$ , and  $\lambda$  parameters, relative to sources with  $0.8 \leq R < 0.9$ , are 461.0%, 10.9%, 138.5%, and 250.0%,

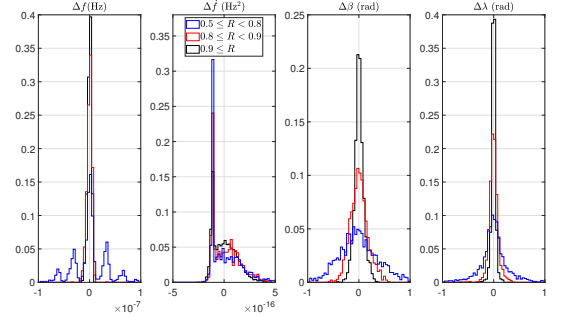


Figure 18. The parameter errors for the intrinsic parameters when  $R$  takes different ranges. The second histogram has a high peak at  $1 \times 10^{-16}$  Hz<sup>2</sup> because some sources have  $\dot{f}$  falling on the negative boundary of the search range, resulting in similar errors.

respectively. Except for  $\dot{f}$ , the errors in the other three parameters have shown a significant increase.

#### D. Computational time

In the first search (without astrophysical models), a total of 849,576 local maxima were explored, necessitating

an average of 310 PSO iterations per search. The average number of  $\mathcal{F}$ -statistic calculations for a local maximum is  $310 \times 40 = 12,400$ , including particles that are deemed invalid due to entering the voids. When determining the radii of the “void” for a local maximum, an additional 120 particles are considered for  $\mathcal{F}$ -statistic calculations. The computation time totaled 816,955 seconds, utilizing 206 Intel(R) Xeon(R) Platinum 8378HC CPU @ 2.60GHz cores concurrently. This corresponds to  $816,955 \times 206$  core-seconds during the search for these local maxima. Furthermore, the time required for removing individual degeneracy noise with the same configuration is approximately 5275 seconds (matlab code).

### E. Discussion

The numbers of confirmed sources in different frequency bins are depicted in Fig. 19. The injection sources refer to signals with  $7 < \text{SNR} < 15$  in the LDC1-4 data. With a low correlation coefficient threshold of  $R_t = 0.5$ , it becomes feasible to detect a substantial portion or approximately half of the injection sources in medium ( $1 \times 10^{-3} \text{ Hz} < f < 4 \times 10^{-3} \text{ Hz}$ ) and low ( $f < 1 \times 10^{-3} \text{ Hz}$ ) frequency ranges. However, in the frequency bins with the highest signal density ( $\sim 2 \times 10^{-3} \text{ Hz}$ ), a notable number of sources remain undetected ( $> 50\%$ ). This observation might be associated with our established stop search criteria or potential interference among the signals themselves. At higher frequencies ( $f > 4 \times 10^{-3} \text{ Hz}$ ), our method demonstrates poor performance. This is attributed to the widening frequency distribution of degeneracy noise as the signal frequency increases. Consequently, it becomes easier to identify the “secondary peaks” (degeneracy noise) produced by the signal rather than the “primary peak” (real signal). To enhance performance at high frequencies, allocating additional computing resources is advisable, and adjustments to our stop search criteria may be necessary. However, by constraining the  $f$  range and conducting a logarithmic search without altering other settings, we successfully identify the sources at higher frequencies. In Fig. 19, the red line serves as the cutoff at  $4 \times 10^{-3} \text{ Hz}$ . On the right side of the line, we utilize the outcomes after removing individual degeneracy noise, restricting the Galactic Latitude, and removing overlapped degeneracy noise in the second search (no cross-validation). On the left side of the line, we employ the confirmed sources obtained through complete find-real- $\mathcal{F}$ -statistic-analysis.

In Fig. 20, we present the Power Spectral Density (PSD) of various datasets. The term “LDC1-4 data” refers to raw data from the LISA Data Challenge, while “instrument noise” represents simulated noise for the LISA mission. “Residual SNR15” denotes LDC1-4 residual data, where injection sources with  $\text{SNR} \geq 15$  have been removed—representing the dataset on which our method operates. The term “Residual confirmed” signifies data from which all confirmed sources ( $R_t = 0.8$ )

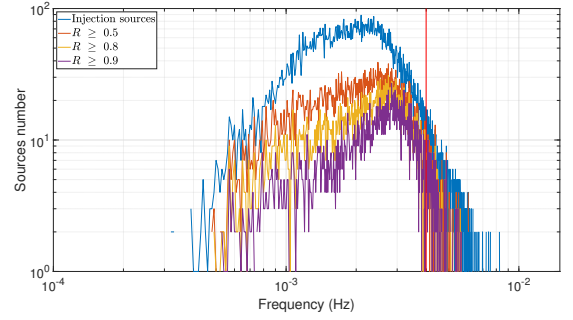


Figure 19. The number of sources in different frequency bins. The injection sources denoting those with  $7 < \text{SNR} < 15$  in LDC1-4 data. The other three colored lines illustrate the count of confirmed sources under different  $R$  ranges to the left of the red vertical line. The red line serves as the cutoff at  $4 \times 10^{-3} \text{ Hz}$ . On the right side of the line, we utilize the outcomes after removing individual degeneracy noise, restricting Galactic Latitude, and removing overlapped degeneracy noise in the second search.

have been subtracted from “Residual SNR15” (as depicted in “remove degeneracy noise” in Fig. 16). We update the amplitude  $\mathcal{A}$  of each source in proportion to the square root of the change in their  $\mathcal{F}$ -statistic values before and after the removal of degeneracy noise. Finally, “Residual SNR7” corresponds to LDC1-4 residual data with injection sources removed based on  $\text{SNR} \geq 7$ , making it an ideal target for our search methodology. There are instances where some sources are not detected, or the reported sources in the results lack accuracy ( $R < 0.8$ ). This phenomenon is attributed to the limitations of the current create voids and find-real- $\mathcal{F}$ -statistic-analysis methods, particularly in resolving signals with very close parameters. For instance, in the case of the signal presented in Fig. 9, where the frequency difference between the two signals is less than  $1 \times df$ , treating them as individual signals becomes challenging. In such scenarios, effectively eliminating degeneracy noise originating from both signals becomes intricate. Even in situations where two or three signals overlap, despite the frequency difference exceeding  $1 \times df$  (as illustrated in Fig. 7(d) and Fig. 10(d)), inconsistencies between the  $\mathcal{F}$ -statistic peak and the binary position add complexity to the subsequent process of removing degeneracy noise. These complexities contribute to the decrease in the DR. To overcome these challenges, other approaches, such as multi-source fitting or leveraging machine learning to analyze the distribution of  $\mathcal{F}$ -statistic values directly in the local maxima, represent promising avenues.

## VII. CONCLUSION

We introduce the LMP SO-CV approach designed for the simultaneous detection of Galactic binary gravitational waves using a space-based GW detector. In deal-



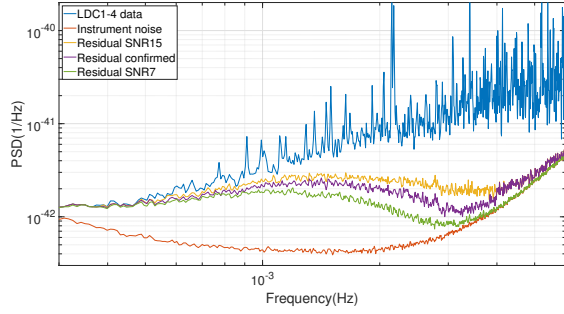


Figure 20. Power spectral density of the different datasets.

ing with the numerous local maxima of the  $\mathcal{F}$ -statistic, the majority of which are degeneracy noise, we employ a find-real- $\mathcal{F}$ -statistic-analysis to effectively remove both degeneracy and instrument noise. We depict the flow chart of our method in Fig. 14. Notably, our approach mitigates the challenges associated with inaccurate subtraction contamination, particularly in the context of resolving low SNR signals (e.g.,  $\text{SNR} < 15$ ), a common difficulty in traditional iterative-subtraction methods. The find-real- $\mathcal{F}$ -statistic-analysis comprises four key steps: 1) eliminating individual signal degeneracy noise, 2) conducting a second search with cross-validation, 3) restricting the Galactic Latitude, and 4) removing overlapped signals degeneracy noise. Following the completion of these steps, our method identifies 8995 signals with  $\text{DR} = 52.3\%$  ( $R_t = 0.8$ ) when applied to the LDC1-4 residual data, which involves subtracting the waveforms of injection sources with  $\text{SNR} \geq 15$ . Alternatively, selecting signals with a change in  $\mathcal{F}$ -statistic value of less than 10% before and after the find-real- $\mathcal{F}$ -statistic-analysis yields 3463 reported sources with  $\text{DR} = 73.1\%$  ( $R_t = 0.8$ ).

Our approach offers a clear advantage in low SNR (e.g.,  $\text{SNR} < 15$ ) and low-frequency ranges (e.g.,  $f < 4 \times 10^{-3}$  Hz). Once the high SNR (e.g.,  $\text{SNR} \geq 15$ ) and high frequency (e.g.,  $f \geq 4 \times 10^{-3}$  Hz) sources have been subtracted, it is worthwhile to continue the search using our method in the residual.

In instances where two or more signals exhibit similarity in their parameters, particularly concerning frequency, the occurrence of overlapped signals is inevitable. The situation becomes intricate when the frequency separation between two signals with comparable Signal-to-Noise Ratio (SNR) is less than five times the minimum frequency resolution achievable during a two-year observation ( $\Delta f < 5 \times \text{df}$ ). Under such circumstances, the  $\mathcal{F}$ -statistic peaks associated with these overlapped signals become complex, introducing challenges in the process of signal resolution. This intricacy adds to the overall challenge of effectively improving the detection rate.

## ACKNOWLEDGMENTS

P. Gao thanks S. D. Mohanty, X. Zhang, J. Ming, S. Zhao and Y. Guo for their invaluable comments and suggestions. Our Local Maxima Particle Swarm Optimization (LMPSO) algorithm is developed based on the PSO script in GBSIEVER method [38] (this PSO code is actually taken from the public repository <https://github.com/mohantysd/SDMBIGDAT19.git>). This work is supported by National Key R&D Program of China (2020YFC2201400), and by the NSFC (No. 11920101003, No. 11922303, No. 12021003 and No. 12005016). X. Fan. is supported by the Fundamental Research Funds for the Central Universities (No.2042022kf1182). Z. Cao was supported by “the Interdiscipline Research Funds of Beijing Normal University” and CAS Project for Young Scientists in Basic Research YSBR-006. We gratefully appreciate the Wuhan Supercomputing Center for the generous computing resources to support our research efforts. We also thank LISA Consortium’s LDC working group for curating and supporting the simulated data used in this study.

## Appendix A: The case study of the method

We employed our method to analyze specific sources and observed its effect. In the Tab. III, we present the parameter of binary  $A$ , which is the same as Fig. 6. For the test, we initially generate the gravitational waveform of binary  $A$  in the LISA data and then introduce instrument noise to create mock data. Since there is only one gravitational wave signal in the data, the task of identifying the signal and removing noise is straightforward. In Fig. 21, we present the parameter positions of the injected source (binary  $A$ ) and the reported source identified by our method in normalized parameter space. It is evident that the positions of the two sources coincide, confirming the accuracy and effectiveness of our search. The correlation coefficient for the reported source is 0.9998.

We also assess the performance of our method in scenarios where two signals overlap. We generate gravitational waveforms for binaries  $A$  and  $B$  in the LISA detector, with the frequency of binary  $B$  incremented by  $4 \times \text{df}$  relative to binary  $A$ . The resulting waveforms, combined with instrument noise, constitute the mock data, corresponding to Fig. 7(c) and Fig. 7(d). Given the overlap of the signals, resolving the two sources becomes more challenging. Due to the low correlation between the two search results during cross-validation, we set the  $R_{ee}$  threshold to 0.7. Ultimately, our method identifies four reported sources, comprising one accurate source, one contaminated source, and two instances of unremoved degeneracy noise. The correlation coefficients for these reported sources are 0.9139, 0.6010, 0.4976, and 0.3510, respectively. The presence of these overlapping sources reduces the detection rate of our search pipeline.



	$f$	$\dot{f}$	$\beta$	$\lambda$	$\mathcal{A}$	$\iota$	$\psi$	$\phi_0$
Binary A	0.002090825	$5.798272 \times 10^{-17}$	0.034327	4.809826	$3.127627 \times 10^{-22}$	1.036248	0.228909	3.22735530717959

Table III. The parameters of the binary A.

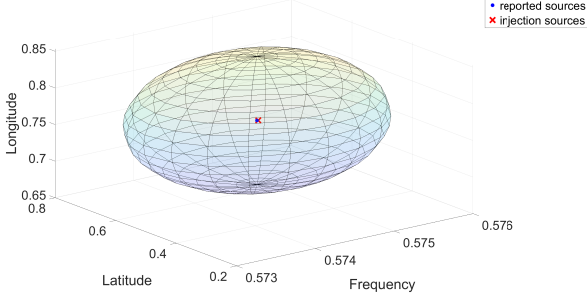


Figure 21. The red cross signifies the position of binary A in the parameter space, while the blue dot represents the reported source identified by our method. The ellipsoid depicts the void with the reported source as the center.

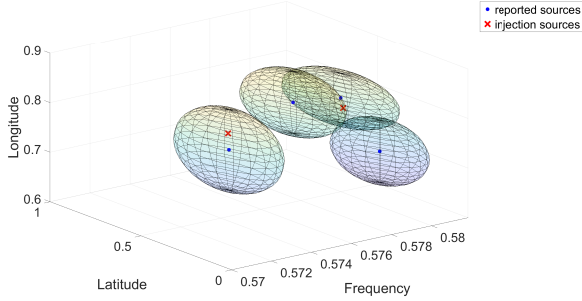


Figure 22. The red cross on the left represents binary A, while the cross on the right represents binary B. The four blue dots represent the reported sources identified by our method. The ellipsoids represent the voids with these reported sources as their centers.

## Appendix B: The overlapping signals from LDC1-4 injection sources

We identified injection sources with  $\text{SNR} \geq 7$  in LDC1-4 data and evaluated the presence of overlapping sources among them for two-year detection. These injection sources were categorized based on SNR thresholds:  $\text{SNR} \geq 15$  or SNR ranging from 7 to 15. In Tab. IV, “Sole” indicates that no other source occurs within its own  $5 \times df$  range, thus not considered an overlapping source. “Two” indicates a source overlapping within the  $5 \times df$  range, as illustrated in Fig. 7(c) and Fig. 7(d). “Three” denotes three continuous overlapping sources, where the frequency interval between two sources is less than  $5 \times df$ , and the interval between one of the sources and the third source is also less than  $5 \times df$ , as depicted in Fig. 10(c) and Fig. 10(d). “Four” indicates four continuous overlapping sources in a sequence, and so on. Among the injection sources with  $\text{SNR} \geq 15$ , we found a maximum of five continuous overlapping sources, with non-overlapping sources comprising 73.6%. For injection sources with SNR between 7 and 15, up to ten continuous overlapping sources were observed, with non-overlapping sources accounting for only 47.2%. It is evident that as SNR decreases, the likelihood of overlapping sources increases, impacting our signal processing and reducing the detection rate of the search pipeline. In fact, we expect as the detection time increases, more and more signals can be resolved, which means that there will be more and more overlap problems.

- 
- [1] J. R. Smith and (for the LIGO Scientific Collaboration), The path to the enhanced and advanced ligo gravitational-wave detectors, *Classical and Quantum Gravity* **26**, 114013 (2009).
  - [2] T. Accadia, F. Acernese, F. Antonucci, P. Astone, G. Ballardin, et al., Status of the virgo project, *Classical and Quantum Gravity* **28**, 114002 (2011).
  - [3] F. Acernese, M. Agathos, L. Aiello, A. Allocca, et al. (Virgo Collaboration), Increasing the astrophysical reach of the advanced virgo detector via the application of squeezed vacuum states of light, *Phys. Rev. Lett.* **123**, 231108 (2019).
  - [4] R. Abbott, T. D. Abbott, S. Abraham, F. Acernese, K. Ackley, A. Adams, C. Adams, R. X. Adhikari, V. B. Adya, C. Affeldt, M. Agathos, K. Agatsuma, et al. (LIGO Scientific Collaboration and Virgo Collaboration), Gwtc-2: Compact binary coalescences observed by ligo and virgo during the first half of the third observing run, *Phys. Rev. X* **11**, 021053 (2021).
  - [5] A. Nitz, S. Kumar, Y.-F. Wang, S. Kasta, S. Wu, M. Schäfer, R. Dhurkunde, and C. Capano, 4-ogc: Catalog of gravitational waves from compact binary mergers, *The Astrophysical Journal* **946**, 59 (2023).
  - [6] B. Abbott, R. Abbott, T. Abbott, M. Abernathy, F. Acernese, K. Ackley, C. Adams, T. Adams, P. Addesso, R. Adhikari, V. Adya, C. Affeldt, M. Agathos, et al., Observation of Gravitational Waves from a Binary Black Hole Merger, *Physical Review Letters* **116**, 061102 (2016).
  - [7] B. P. Abbott, R. Abbott, T. D. Abbott, F. Acernese, K. Ackley, C. Adams, T. Adams, P. Addesso, et al. (LIGO Scientific Collaboration and Virgo Collabora-

Injection sources' SNR	Sole	Two	Three	Four	Five	Six	Seven	Eight	Nine	Ten	Total number
$\geq 15$	8079	2208	561	124	10	0	0	0	0	0	10982
$7 \sim 15$	7874	4344	2175	1136	560	318	154	72	45	20	16698

Table IV. The number of overlapping signals from LDC1-4 injection sources is categorized as follows: “Sole” denotes no overlapping source. “Two” indicates that the frequency interval between two sources is less than  $5 \times df$ , resulting in their overlap. “Three” implies that not only the frequency interval between two sources is less than  $5 \times df$ , but also the frequency interval between one of the sources and the third source is less than  $5 \times df$ , and so forth.

- tion), Gw170817: Observation of gravitational waves from a binary neutron star inspiral, *Phys. Rev. Lett.* **119**, 161101 (2017).
- [8] R. Abbott, T. D. Abbott, S. Abraham, F. Acernese, K. Ackley, A. Adams, C. Adams, R. X. Adhikari, V. B. Adya, *et al.*, Observation of gravitational waves from two neutron star–black hole coalescences, *The Astrophysical Journal Letters* **915**, L5 (2021).
- [9] H. Miao, H. Yang, and D. Martynov, Towards the design of gravitational-wave detectors for probing neutron-star physics, *Phys. Rev. D* **98**, 044044 (2018).
- [10] D. Martynov, H. Miao, H. Yang, F. H. Vivanco, E. Thrane, R. Smith, P. Lasky, W. E. East, R. Adhikari, A. Bauswein, A. Brooks, Y. Chen, T. Corbitt, A. Freise, H. Grote, Y. Levin, C. Zhao, and A. Vecchio, Exploring the sensitivity of gravitational wave detectors to neutron star physics, *Phys. Rev. D* **99**, 102004 (2019).
- [11] Y. P. Z. W. M. C. M. W. F. Z. J. Z. Z.-H. Z. Junlang Li, Fangfei Liu, Detecting gravitational wave with an interferometric seismometer array on lunar nearside, *SCIENCE CHINA Physics, Mechanics & Astronomy* **66** (2023).
- [12] H. Audley, S. Babak, J. Baker, E. Barausse, P. Bender, E. Berti, P. Binetruy, M. Born, D. Bortoluzzi, J. Camp, C. Caprini, V. Cardoso, M. Colpi, J. Conklin, N. Cornish, C. Cutler, K. Danzmann, R. Dolesi, L. Ferraioli, and C. F. Sopuerta, Laser interferometer space antenna, (2017).
- [13] J. Baker, J. Bellovary, P. Bender, E. Berti, R. Caldwell, J. Camp, J. Conklin, N. Cornish, C. Cutler, R. DeRosa, M. Eracleous, E. Ferrara, S. Francis, M. Hewitson, K. holley bockelmann, A. Hornschemeier, C. Hogan, B. Kamai, B. Kelly, and J. Ziemer, The laser interferometer space antenna: Unveiling the millihertz gravitational wave sky (2019).
- [14] G. Agazie, M. F. Alam, A. Anumalapudi, A. M. Archibald, Z. Arzoumanian, P. T. Baker, L. Blecha, V. Bonidie, *et al.*, The nanograv 15 yr data set: Observations and timing of 68 millisecond pulsars, *The Astrophysical Journal Letters* **951**, L9 (2023).
- [15] A. Afzal, G. Agazie, A. Anumalapudi, A. M. Archibald, Z. Arzoumanian, P. T. Baker, B. Bécsy, J. J. Blanco-Pillado, L. Blecha, K. K. Boddy, A. Brazier, *et al.*, The nanograv 15 yr data set: Search for signals from new physics, *The Astrophysical Journal Letters* **951**, L11 (2023).
- [16] EPTA Collaboration, Antoniadis, J., Babak, S., Bak Nielsen, A.-S., Bassa, C. G., Berthureau, A., *et al.*, The second data release from the european pulsar timing array - i. the dataset and timing analysis, *A&A* **678**, A48 (2023).
- [17] H. Xu, S. Chen, Y. Guo, J. Jiang, B. Wang, J. Xu, Z. Xue, R. N. Caballero, J. Yuan, Y. Xu, *et al.*, Searching for the nano-hertz stochastic gravitational wave background with the chinese pulsar timing array data release i, *Research in Astronomy and Astrophysics* **23**, 075024 (2023).
- [18] D. J. Reardon, A. Zic, R. M. Shannon, G. B. Hobbs, M. Bailes, V. D. Marco, A. Kapur, *et al.*, Search for an isotropic gravitational-wave background with the parkes pulsar timing array, *The Astrophysical Journal Letters* **951**, L6 (2023).
- [19] G. Agazie, A. Anumalapudi, A. M. Archibald, Z. Arzoumanian, P. T. Baker, B. Bécsy, L. Blecha, A. Brazier, P. R. Brook, S. Burke-Spolaor, R. Burnette, *et al.*, The nanograv 15 yr data set: Evidence for a gravitational-wave background, *The Astrophysical Journal Letters* **951**, L8 (2023).
- [20] X. Gong, S. Xu, S. Bai, Z. Cao, G. Chen, Y. Chen, X. He, *et al.*, A scientific case study of an advanced lisa mission, *Classical and Quantum Gravity* **28**, 094012 (2011).
- [21] W.-R. Hu and Y.-L. Wu, The Taiji Program in Space for gravitational wave physics and the nature of gravity, *National Science Review* **4**, 685 (2017).
- [22] Y.-L. Wu, Z. Luo, J.-Y. Wang, M. Bai, W. Bian, H.-W. Cai, R.-G. Cai, Z.-M. Cai, J. Cao, B. Chen, D.-J. Chen, G.-F. Chen, K. Chen, L. Chen, S. Chen, M.-W. Chen, W.-B. Chen, Y. Chen, Z.-Y. Chen, and Z.-M. Zou, Taiji program in space for gravitational universe with the first run key technologies test in taiji-1, *International Journal of Modern Physics A* **36**, 2102002 (2021).
- [23] The Taiji Scientific Collaboration, Y.-L. Wu, Z.-R. Luo, J.-Y. Wang, M. Bai, W. Bian, R.-G. Cai, Z.-M. Cai, J. Cao, D.-J. Chen, L. Chen, L.-S. Chen, M.-W. Chen, *et al.*, China’s first step towards probing the expanding universe and the nature of gravity using a space borne gravitational wave antenna, *Communications Physics* **4**, 34 (2021).
- [24] Z. Luo, Y. Wang, Y. Wu, W. Hu, and G. Jin, The taiji program: A concise overview, *Progress of Theoretical and Experimental Physics* **ptaa083** (2020).
- [25] J. Luo, L.-S. Chen, H.-Z. Duan, Y.-G. Gong, S. Hu, J. Ji, Q. Liu, J. Mei, V. Milyukov, M. Sazhin, C.-G. Shao, V. T. Toth, H.-B. Tu, Y. Wang, Y. Wang, H.-C. Yeh, M.-S. Zhan, Y. Zhang, V. Zharov, and Z.-B. Zhou, TianQin: a space-borne gravitational wave detector, *Classical and Quantum Gravity* **33**, 035010 (2016).
- [26] Y.-M. Hu, J. Mei, and J. Luo, Science prospects for space-borne gravitational-wave missions, *National Science Review* **4**, 683 (2017).
- [27] J. Mei, Y.-Z. Bai, J. Bao, E. Barausse, L. Cai, E. Canuto, B. Cao, W.-M. Chen, *et al.*, The TianQin project: current progress on science and technology, *Progress of Theoretical and Experimental Physics* **10.1093/ptep/ptaa114** (2020), arXiv: 2008.10332.

- [28] J. Luo, Y.-Z. Bai, L. Cai, B. Cao, W.-M. Chen, Y. Chen, D.-C. Cheng, Y.-W. Ding, et al., The first round result from the TianQin-1 satellite, *Classical and Quantum Gravity* **37**, 185013 (2020).
- [29] T. Robson, N. J. Cornish, and C. Liu, The construction and use of LISA sensitivity curves, *Classical and Quantum Gravity* **36**, 105011 (2019).
- [30] J. A. Edlund, M. Tinto, A. Królak, and G. Nelemans, Simulation of the white dwarf–white dwarf galactic background in the LISA data, *Classical and Quantum Gravity* **22**, S913 (2005).
- [31] S. D. Mohanty and R. K. Nayak, Tomographic approach to resolving the distribution of LISA Galactic binaries, *Physical Review D* **73**, 083006 (2006).
- [32] J. Crowder and N. J. Cornish, Extracting galactic binary signals from the first round of Mock LISA Data Challenges, *Classical and Quantum Gravity* **24**, S575 (2007).
- [33] R. Prix and J. T. Whelan, F-statistic search for white-dwarf binaries in the first mock lisa data challenge, *Classical and Quantum Gravity* **24**, S565 (2007).
- [34] J. Crowder and N. J. Cornish, Solution to the galactic foreground problem for LISA, *Physical Review D* **75**, 043008 (2007).
- [35] T. B. Littenberg, Detection pipeline for Galactic binaries in LISA data, *Physical Review D* **84**, 063009 (2011).
- [36] A. Blaut, S. Babak, and A. Królak, Mock LISA data challenge for the Galactic white dwarf binaries, *Physical Review D* **81**, 063008 (2010).
- [37] T. B. Littenberg, N. J. Cornish, K. Lackeos, and T. Robson, Global analysis of the gravitational wave signal from Galactic binaries, *Physical Review D* **101**, 123021 (2020).
- [38] X.-H. Zhang, S. D. Mohanty, X.-B. Zou, and Y.-X. Liu, Resolving Galactic binaries in LISA data using particle swarm optimization and cross-validation, *Physical Review D* **104**, 024023 (2021).
- [39] S. H. Strub, L. Ferraioli, C. Schmeltzbach, S. C. Stähler, and D. Giardini, Bayesian parameter estimation of galactic binaries in lisa data with gaussian process regression, *Phys. Rev. D* **106**, 062003 (2022).
- [40] Y. Lu, E.-K. Li, Y.-M. Hu, J. dong Zhang, and J. Mei, An implementation of galactic white dwarf binary data analysis for mldc-3.1, *Research in Astronomy and Astrophysics* **23**, 015022 (2023).
- [41] X.-H. Zhang, S.-D. Zhao, S. D. Mohanty, and Y.-X. Liu, Resolving galactic binaries using a network of space-borne gravitational wave detectors, *Phys. Rev. D* **106**, 102004 (2022).
- [42] P. Gao, X.-L. Fan, Z.-J. Cao, and X.-H. Zhang, Fast resolution of Galactic binaries in LISA data, *Physical Review D* **107**, 123029 (2023).
- [43] K. Lackeos, T. B. Littenberg, N. J. Cornish, and J. I. Thorpe, The LISA Data Challenge Radler analysis and time-dependent ultra-compact binary catalogues, *Astronomy & Astrophysics* **678**, A123 (2023).
- [44] S. H. Strub, L. Ferraioli, C. Schmeltzbach, S. C. Stähler, and D. Giardini, Accelerating global parameter estimation of gravitational waves from Galactic binaries using a genetic algorithm and GPUs, *Phys. Rev. D* **108**, 103018 (2023), [arXiv:2307.03763 \[astro-ph.IM\]](https://arxiv.org/abs/2307.03763).
- [45] LDC-manual-Sangria.pdf, <https://lisa-ldc.lal.in2p3.fr/> (2020).
- [46] M. Tinto, F. B. Estabrook, and J. W. Armstrong, Time-delay interferometry for LISA, *Physical Review D* **65**, 082003 (2002).
- [47] M. Tinto and S. V. Dhurandhar, Time-Delay Interferometry, *Living Reviews in Relativity* **17**, 6 (2014).
- [48] J. W. Armstrong, F. B. Estabrook, and M. Tinto, Time-Delay Interferometry for Space-based Gravitational Wave Searches, *The Astrophysical Journal* **527**, 814 (1999).
- [49] M. Tinto, F. B. Estabrook, and J. W. Armstrong, Time delay interferometry with moving spacecraft arrays, *Physical Review D* **69**, 082001 (2004).
- [50] P. Jaranowski, A. Królak, and B. F. Schutz, Data analysis of gravitational-wave signals from spinning neutron stars: The signal and its detection, *Physical Review D* **58**, 063001 (1998).
- [51] N. J. Cornish and S. L. Larson, LISA data analysis: Source identification and subtraction, *Physical Review D* **67**, 103001 (2003).
- [52] N. Cornish and S. Larson, LISA data analysis I: Doppler demodulation, *Classical and Quantum Gravity* **20**, S163 (2003), [arXiv:gr-qc/0206017](https://arxiv.org/abs/gr-qc/0206017).
- [53] J. Kennedy and R. Eberhart, Particle swarm optimization, *International Conference on Neural Networks*, **4**, 1942 (1995).
- [54] A. G. Gad, Particle Swarm Optimization Algorithm and Its Applications: A Systematic Review, *Archives of Computational Methods in Engineering* **29**, 2531 (2022).
- [55] M. Kilic, C. Allende Prieto, W. R. Brown, and D. Koester, The Lowest Mass White Dwarf, *The Astrophysical Journal* **660**, 1451 (2007).